Astronomy & Astrophysics

The cerium content of the Milky Way as revealed by *Gaia* DR3 GSP-Spec abundances

G. Contursi[1], P. de Laverny[1], A. Recio-Blanco[1], E. Spitoni[1], P. A. Palicio[1], E. Poggio[1], V. Grisoni[2,3],
G. Cescutti[4,5,6], F. Matteucci[4,5,6], L. Spina[7], M. A. Álvarez[8], G. Kordopatis[1], C. Ordenovic[1],
I. Oreshina-Slezak[1], and H. Zhao[1,9]

1 Université Côte d'Azur, Observatoire de la Côte d'Azur, CNRS, Laboratoire Lagrange, Bd de l'Observatoire, CS 34229,
   06304 Nice cedex 4, France
   e-mail: gabriele.contursi@oca.eu
2 Dipartimento di Fisica e Astronomia, Università degli Studi di Bologna, Via Gobetti 93/2, 40129 Bologna, Italy
3 INAF, Osservatorio di Astrofisica e Scienza dello Spazio, Via Gobetti 93/3, 40129 Bologna, Italy
4 Dipartimento di Fisica, Sezione di Astronomia, Università di Trieste, via G.B. Tiepolo 11, 34131 Trieste, Italy
5 INAF Osservatorio Astronomico di Trieste, via G.B. Tiepolo 11, 34131 Trieste, Italy
6 INFN Sezione di Trieste, via Valerio 2, 34134 Trieste, Italy
7 INAF – Osservatorio astronomico di Padova, Vicolo Osservatorio 5, 35122 Padova, Italy
8 CIGUS CITIC – Department of Computer Science and Information Technologies, University of A Coruña, Campus de Elviña s/n,
   A Coruña 15071, Spain
9 Purple Mountain Observatory, Chinese Academy of Sciences, Nanjing 210023, PR China

Received 11 July 2022 / Accepted 16 November 2022

ABSTRACT

Context. The recent *Gaia* third data release contains a homogeneous analysis of millions of high-quality Radial Velocity Spectrometer (RVS) stellar spectra by the GSP-Spec module. This led to the estimation of millions of individual chemical abundances and allows us to chemically map the Milky Way. The published GSP-Spec abundances include three heavy elements produced by neutron-captures in stellar interiors: Ce, Zr, and Nd.

Aims. We study the Galactic content in cerium based on these *Gaia*/RVS data and discuss the chemical evolution of this element.

Methods. We used a sample of about 30 000 local thermal equilibrium Ce abundances, selected after applying different combinations of GSP-Spec flags. Based on the *Gaia* DR3 astrometric data and radial velocities, we explore the cerium content in the Milky Way and, in particular, in its halo and disc components.

Results. The high quality of the Ce GSP-Spec abundances is quantified through literature comparisons. We found a rather flat [Ce/Fe] versus [M/H] trend. We also found a flat radial gradient in the disc derived from field stars and, independently, from about 50 open clusters. This agrees with previous studies. The [Ce/Fe] vertical gradient was also estimated. We also report an increasing [Ce/Ca] versus [Ca/H] in the disc, illustrating the late contribution of asymptotic giant branch stars with respect to supernovae of type II. Our cerium abundances in the disc, including the young massive population, are well reproduced by a new three-infall chemical evolution model. In the halo population, the M 4 globular cluster is found to be enriched in cerium. Moreover, 11 stars with cerium abundances belonging to the Thamnos, Helmi Stream, and Gaia-Sausage-Enceladus accreted systems were identified from chemo-dynamical diagnostics. We found that the Helmi Stream might be slightly underabundant in cerium compared to the two other systems.

Conclusions. This work illustrates the high quality of the GSP-Spec chemical abundances, which significantly contribute to unveiling the heavy-element evolution history of the Milky Way.

Key words. Galaxy: abundances – stars: abundances – Galaxy: disk – Galaxy: halo – Galaxy: evolution

1. Introduction

Our understanding of the Milky Way has made a great leap forwards through the different data releases of the *Gaia* mission. The third release (Gaia Collaboration 2023b) consists of a major and unique step because it includes a large variety of new data products, including, in particular, an extensive characterisation of the *Gaia* sources. In this context, the module called general stellar parametrizer from spectroscopy (GSP-Spec hereafter; see Gaia Collaboration 2023a) has estimated atmospheric parameters (effective temperature $T_{\rm eff}$, surface gravity $\log(g)$, global metallicity [M/H], and abundances of α-elements with respect

to iron [α/Fe]) as well as individual chemical abundances of up to a dozen elements[1] for about 5.6 million stars that have been observed by the Radial Velocity Spectrometer (RVS hereafter; Cropper et al. 2018; Katz et al. 2023).

Three of these 13 chemical elements are produced by neutron capture in the inner layers of some specific stages of stellar evolution: zirconium ($Z = 40$), cerium ($Z = 58$), and neodynium ($Z = 60$). According to the seminal work of Burbidge et al.

---

[1] See https://www.cosmos.esa.int/web/gaia/iow_20210709. These elements are N, Mg, Si, S, Ca, Ti, Fe I, Fe II, Ni, Zr, Ce, and Nd.

(1957), neutron capture occurs through two main processes: the rapid (*r*-) and slow (*s*-) processes (slow and rapid referring to the timescale of the neutron captures with respect to the β-decay). The latter takes place in lower neutron densities and on longer timescales than the *r*-process. The main formation sites of the *r*-process elements are still under discussion: merging of neutron stars or of neutron star - black hole binary systems (respectively Freiburghaus et al. 1999; Surman et al. 2008), neutrino-induced winds from the core-collapse of supernovae (Woosley et al. 1994), and/or rotating polar jets from core-collapse supernovae (Nishimura et al. 2006).

The formation sites of the *s*-process, in contrast, are better understood. The distribution of solar abundances shows three peaks located around the atomic mass numbers A = 90, 138, and 208. Sr, Y, and Zr represent the first peak, Ba, La, and Ce the second peak, and Pb the third peak. Even though all these elements are mainly formed via *s*-process (Prantzos et al. 2018), their formation sites can differ. The *s*-process can be decomposed into three sub-processes, each of which populates a different peak (see Kappeler et al. 1989, and references therein). First, massive stars ($\gtrsim 8$–$10\,M_\odot$) preferentially cause the so-called weak process (especially producing first peak elements), where neutrons are mainly provided by the $^{22}\text{Ne}(\alpha, \text{n})^{25}\text{Mg}$ reaction in the convective He-burning core and C-burning shell (Peters 1968; Lamb et al. 1977; Pignatari et al. 2010). On the other hand, low- and intermediate-mass Asymptotic giant branch stars at solar metallicity produce the so-called main *s*-process such as Ce and Nd through neutrons that are mainly produced by the $^{13}\text{C}(\alpha,\text{n})^{16}\text{O}$ reaction (Arlandini et al. 1999; Busso et al. 1999; Karakas & Lattanzio 2014; Bisterzo et al. 2011, 2015). This reaction takes place in the so-called ^{13}C-pocket, between the H- and He-burning shells. This ^{13}C pocket is formed through a sequence reaction $^{12}\text{C}(p,\gamma)^{13}\text{N}(\beta^+)^{13}\text{C}$ through the partial mixing of protons from the convective H-rich envelope into the ^{12}C region during the third dredge-up. The $^{22}\text{Ne}(\alpha, \text{n})^{25}\text{Mg}$ reaction also contributes to the convective thermal pulse. Moreover, we note that rotating massive stars at low metallicity ([Fe/H] $< -0.5\,\text{dex}$) seem to have an impact on the main *s*- process elements (Prantzos et al. 2018). Finally, low-metallicity low-mass AGB can produce elements of the third peak (e.g. Pb) through the strong *s*-process (Clayton & Rassbach 1967; Gallino et al. 1998; Travaglio et al. 2001)

However, this rather simple picture is blurred by the fact that neutron-capture elements can be produced by a combination of the *s*- and *r*- processes. For instance, Arlandini et al. (1999) found that at the epoch of the Solar System formation, cerium could come at a level of 77% from *s*-process production. This was later confirmed by Bisterzo et al. (2016) and Prantzos et al. (2018), who report a *s*-process contribution of about 80%.

For all these reasons, studying the Ce content in the Milky Way allows us to probe its different production sites and, in particular, the main *s*- process. Several studies of neutron-capture elements and more especially, of cerium abundances in the Galactic disc, can be found in the literature, for instance, Reddy et al. (2006), Mishenina et al. (2013), Battistini & Bensby (2016), Delgado Mena et al. (2017), Forsberg et al. (2019), Griffith et al. (2021) for field star studies, and Magrini et al. (2018), Spina et al. (2021), Sales-Silva et al. (2022) for open clusters. Global flat trends of [Ce/Fe] versus [M/H] were found in most works, even though some report a small decreasing trend for high [Fe/H] values (Mashonkina et al. 2007). This trend agrees with chemical models (Prantzos et al. 2018; Grisoni et al. 2020). Moreover, a correlation between cerium abundances and ages has been proposed based on open clusters (Sales-Silva et al. 2022), where

[Ce/Fe] appears to decrease with age up to 8 Gyr. A similar trend was obtained for field stars (Battistini & Bensby 2016). They additionally found an increase in [Ce/Fe] with ages older than 8 Gyr.

With the recent delivery of the third *Gaia* data release, these studies can be extended to a much larger stellar sample. The aim of the present paper is therefore to complement the first description of Ce based on the *Gaia* GSP-Spec abundances that was presented by Gaia Collaboration (2023a). This work is composed as follows. Section 2 describes the selection of the sample of Ce abundances, and Sect. 3 presents its spatial, chemical, and dynamical properties. Section 4 presents the Galactic disc content in cerium with the derivation of radial and vertical gradients, the comparison with a new chemical evolution model, and the Ce content of open clusters. Then, Sect. 5 explores Ce abundances in the Galactic halo and, in particular, in the M 4 globular cluster and in accreted dwarf galaxies and stellar streams. Finally, the conclusions of this work are presented in Sect. 6.

2. Sample stars of cerium abundances

This section presents the recently published *Gaia* DR3 cerium abundances. We select the best working samples for further analysis (see Appendix A for the corresponding catalogue queries).

2.1. Gaia GSP-Spec local thermal equilibrium cerium abundances

First, we briefly recall that the chemical analysis of the *Gaia*-RVS spectra ($R \sim 11\,500$) was performed by the GSP-Spec module (Recio-Blanco et al. 2023) through the GAUGUIN algorithm (Bijaoui 2012; Recio-Blanco et al. 2016) and a specific grid of synthetic spectra covering the whole stellar atmospheric parameters space and with varying Ce abundances. Briefly, to derive chemical abundances, GAUGUIN builds a reference grid spectrum (1D) from this large 5D cerium grid that is interpolated at the atmospheric parameters of the analysed star. These atmospheric parameters are provided by the MatisseGauguin method (see Sect. 6 of Recio-Blanco et al. (2023) for more details). The observed spectrum of the analysed star is normalised, and a second normalisation around the line is then performed to readjust the continuum locally (Santos-Peral et al. 2020; Recio-Blanco et al. 2023). Finally, the minimum of the quadratic distance between the observed and reference spectra is computed in a wavelength range close to the line. This provides the initial guess of the Ce abundance, from which the Gauss-Newton algorithm obtains the final abundance. The second normalisation and abundance windows from which the cerium abundances are derived are provided in Table B.1. of Recio-Blanco et al. (2023). The derived local thermodynamical equilibrium (LTE) abundances rely on the line data of Contursi et al. (2021) and assume Grevesse et al. (2007) solar abundances.

Cerium abundances are determined from a triplet of Ce II lines centred around 851.375 nm (in vacuum). Table 1 reports the atomic data of this triplet that we adopted for the analysis: air and vacuum wavelengths[2], excitation energy of the lower level, and oscillator strength. These atomic data were not calibrated astrophysically. Moreover, for some specific combinations of atmospheric parameters, this cerium triplet might be slightly blended with a weak CN line whose central wavelength is about 851.25 nm.

---

[2] The conversion between air and vacuum wavelength was made following Birch & Downs (1994).

Table 1. Adopted cerium line data.

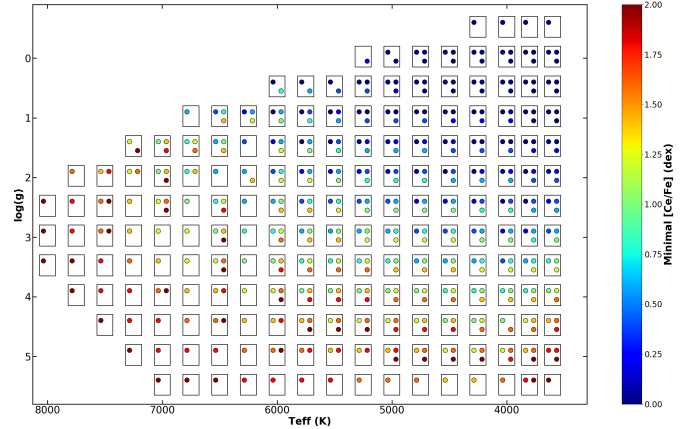| Element	λ_{air} (nm)	λ_{vac} (nm)	E (eV)	$\log(gf)$
Ce II	851.1337	851.3676	0.357	−2.530
Ce II	851.1473	851.3812	2.004	−2.120
Ce II	851.1521	851.3859	0.328	−2.840

Fig. 1. Kiel diagram colour-coded with the lowest cerium abundance (in dex) that could be detected in a spectrum whose (normalised) line core flux is 0.5% deeper than that of a reference spectrum with [Ce/Fe] = −2.0 dex. For each combination of effective temperature and surface gravity, we estimated this lowest cerium abundance for three values of [M/H]: 0.0, −0.5, and −1.0 dex (from top to bottom and left to right in each small square).

An example of this cerium feature is provided in Fig. 9 of Recio-Blanco et al. (2023). The detectability of the cerium triplet is illustrated in Fig. 1, which presents a Kiel diagram colour-coded with the minimum cerium abundance (in dex) that could be measured for metallicities varying between −1.0 to 0.0 dex. This was estimated from the grid of synthetic spectra in which we searched for the Ce abundance corresponding to a (normalised) flux decrease of 0.5% at the Ce line core with respect to a reference spectrum with [Ce/Fe] = −2.0 dex (i.e. no Ce and the lowest cerium abundance in the grid of reference spectra). The cerium lines are more easily detectable in AGB and RGB stars ([Ce/Fe] > 0 dex), whereas higher cerium abundances are required for a possible detection in dwarf stars. This may lead to the observational biases that are discussed in Sects. 3.1 and 4.1.

We recall that according to Lawler et al. (2009), cerium has four main stable isotopes, and two of them are dominant (88.45% for ^{140}Ce and 11.11% for ^{142}Ce). Then, 0.19% and 0.25% of Ce are found in ^{146}Ce and ^{138}Ce, respectively.

Together with other chemical abundances, GSP-Spec provides several quality flags that are recommended for selecting the best data. These flags are related to several effects that could affect the stellar parametrisation, for instance, possible biases induced by radial velocity uncertainties, rotational broadening, or flux noise. Moreover, two flags specifically refer to the determination of the cerium chemical abundance (Ce*UpLim* and Ce*Uncer*). The Ce*UpLim* flag is an indicator of the line depth with respect to noise level, which corresponds to the detectability limit defined as the upper limit. The smaller this flag, the better the measurement. The Ce*Uncer* flag is defined as the reliability of the abundance uncertainty considering the atmospheric parameters and S/N. We refer to Recio-Blanco et al. (2023) for a complete definition of these flags.

Out of the ∼5.5 million stars parametrised by GSP-Spec, 103 948 have a cerium abundance, without considering any flag restriction (we refer to this entire Ce catalogue as the complete sample hereafter). As this study aims to describe the largest possible sample with the most accurate Ce measurements, we applied some flag restrictions to define our working samples and compare the GSP-Spec [Ce/Fe] values with the literature values.

2.2. Comparison catalogues of cerium abundances

In order to validate the GSP-Spec cerium abundances, they were compared to the abundances of APOGEE-DR17 (Abdurro'uf et al. 2022), Forsberg et al. (2019; APOGEE and F19 hereafter, respectively), and GALAH DR3 (Buder et al. 2021).

We first note that there are no GALAH stars in common with F19 after the recommended GALAH flag values were applied ($snr\_c3\_iraf > 30$, $flag\_sp == 0$, $flag\_fe\_h == 0$ and $flag\_Ce\_fe == 0$). Nevertheless, we compare below our GSP-Spec cerium abundances with the abundance from GALAH in

Sect. 2.4. These GALAH Ce abundances were derived from one cerium line around 477.3941 nm (air) from spectra with $R \sim 28\,000$. A zero-point calibration was applied. Using these recommended flags, we found 278 163 GALAH cerium abundances.

The F19 cerium abundance sample is composed of 336 stars observed at highweresolution ($R \sim 67\,000$). Their abundances are obtained from a Ce II line located at 604.3373 nm in the air, adopting solar composition from Grevesse et al. (2015).

APOGEE cerium abundances were derived from spectra with $R \sim 22\,500$ and $S/N > 100$, using multiple cerium lines. For our comparison purpose, we selected the best APOGEE non-calibrated Ce abundances. We then filtered all stars with APOGEE ANDFLAGS, ASPCAPFLAGS, RV_FLAGS, and STARFLAGS ≠ 0. We also removed stars with a non-zero third binary digit of the EXTRATARG flag and a non-zero value for the sixth and twenty-sixth binary digits of each member of PARAMFLAG tuple. Finally, we kept only APOGEE cerium abundances with an uncertainty smaller than 0.2 dex and found 53 310 stars. Our flag selection is the recommended optimized version of APOGEE flags. The F19 and APOGEE samples can be compared between each other. We found 32 stars with high-quality Ce abundances in common. They have a mean difference of −0.14 dex, in the sense APOGEE minus F19, indicating that the two studies are probably not at the same reference level. Calibrated APOGEE abundances lead to a larger difference of −0.20 dex. We therefore consider only non-calibrated APOGEE abundances in the following. F19 Ce abundances are indeed almost always higher than those from APOGEE. This difference is even larger for some APOGEE cerium-poor stars that are found to be ∼0.3–0.4 dex more enriched in Ce by F19, although no significant differences in atmospheric parameters are present. Nevertheless, the standard deviation of the Ce abundance differences in the two samples is equal to 0.13 dex, revealing a rather good agreement between the two studies. We note that similar systematic differences (different reference scales) of cerium abundances at solar metallicity have been reported by F19 when they compared their own abundances with those of Battistini & Bensby (2016).

Table 2. Comparison (mean and standard deviation of the differences) between GSP-Spec cerium abundances and those of F19, APOGEE, and GALAH for different samples of Ce GSP-Spec abundances.

	Strict Select.			Low-Uncer. Samp.			Complete Samp.		
	F19	APO	GLH	F19	APO	GLH	F19	APO	GLH
Mean	0.03	−0.06	–	0.00	−0.16	−0.31	0.00	−0.27	−0.44
Std	0.05	0.09	–	0.15	0.25	0.20	0.15	0.30	0.32
N_{comp}	9	2	0	105	101	44	122	187	333
N_{Ce}		493			29 991			103 948	

Notes. The [Ce/Fe] mean values are computed in the sense literature minus GSP-Spec. N_{comp} indicates the number of stars found for the comparison, and N_{Ce} is the total number of GSP-Spec stars with Ce abundances when the corresponding flag selection was applied (see text for more details).

2.3. Definition of the low-uncertainty sample of GSP-Spec Ce abundances

We then compare in Table 2 the differences between GSP-Spec cerium abundances and those of F19, APOGEE, and GALAH for three possible *flags_gspspec* selections. We also indicate the number of stars (N_{col}) used for the comparison, as well as the total number of selected GSP-Spec stars (N_{Ce}) when the considered flags were applied.

We first show this comparison in the left column by adopting stars for which (i) all their *flags_gspspec* = 0 (including those related to Ce abundances), (ii) Ce uncertainties smaller than 0.2 dex (estimated from Monte Carlo simulations; see Recio-Blanco et al. 2023), (iii) *vbroad* ≤ 13 km s^{-1} (since deriving accurate chemical abundances can become difficult for fast-rotating stars)[3], (iv) T_{eff} ≤ 5400 K (tests with synthetic spectra show that the Ce lines become too weak to be detected in hotter star spectra), and (v) $\log(g)$ ≤ 3.5 (tests with synthetic spectra revealed that the Ce line becomes difficult to analyse in dwarf stars)[4]. We finally found 493 stars that satisfied these criteria (referred to as the strict selection hereafter). Among them, we found only 9, 2 and 0 stars in common with F19, APOGEE and GALAH, respectively. An excellent agreement between [Ce/Fe] GSP-Spec, F19 and APOGEE values is found.

For comparison purpose, we provide a similar comparison in the right column of Table 2, but considering the complete sample of Ce abundances. The number of stars in common is much larger, and the agreement between GSP-Spec and F19 is still very good (no bias and dispersion equal to 0.15 dex). In contrast, the agreement with APOGEE and GALAH is worse. The large bias can be explained by the fact that GSP-Spec, APOGEE, and GALAH Ce abundances are not on the same scale (as is also the case for F19 and APOGEE, as mentioned in the previous subsection). The dispersion is also larger, maybe because the some of APOGEE stars found in GSP-Spec are fainter than those in F19.

From these considerations and in order to select a large enough but still accurate sample of Ce abundances, we defined a specific combination of the GSP-Spec flags by relaxing the

extrapol and *KMgiantPar* flags together with those specifically related to Ce abundances. Briefly, the *extrapol* flag indicates if the GSP-Spec atmospheric parameters are extrapolated beyond the limits of the reference grid and *KMgiantPar* refers to extremely cool giant stars whose T_{eff} and $\log(g)$ have been corrected and set to given specific values because of parametrisation issues. We again refer to Recio-Blanco et al. (2023) for a complete definition of these flags. Our best combination was found by adopting *CeUpLim* ≤ 2, *CeUncer* ≤ 1 and *extrapol* ≤ 1. We also fixed *KMgiantPar* ≤ 1, which is associated with a goodness of fit (referred as gof hereafter; see Recio-Blanco et al. 2023, for its definition) lower than −3.75. All the other flags were set to 0 to ensure a good stellar parametrisation. As for the strict selection sample, we also only selected stars with *vbroad* ≤ 13 km s^{-1}, Ce uncertainties ≤0.2 dex, T_{eff} ≤ 5400^{-1} K, and $\log(g)$ < 3.5. This low-uncertainty sample contains 29 991 stars with accurate measurements of the Ce abundances.

2.4. Comparison of the low-uncertainty sample with the reference catalogues

In this low-uncertainty sample, we found 105, 101, and 44 stars in common with F19, APOGEE, and GALAH, all with a GSP-Spec S/N higher than 55. The comparisons between these studies are illustrated in Fig. 2. The agreement between this low-uncertainty sample and F19 is excellent (no bias and dispersion of 0.15 dex), whereas the comparison with APOGEE is good with a bias identical to the bias between F19 and APOGEE, together with a larger dispersion of 0.25 dex. We note that most of the GALAH and APOGEE low Ce abundances seem to be systematically underestimated compared to those from $GSP-Spec$ and F19. The agreement with GALAH and APOGEE is indeed much better when their lowest Ce abundances are rejected: keeping only GALAH and APOGEE stars with [Ce/Fe] > −0.15 dex leads to a mean difference with respect to GSP-Spec equal to −0.09 and −0.22 dex, respectively. The standard deviation with respect to GSP-Spec becomes equal to 0.18 and 0.18 dex, respectively.

The excellent agreement between GSP-Spec and F19 might be explained by the high quality of these spectra: high spectral resolution, and S/N for F19 and high S/N for GSP-Spec. APOGEE stars in common with GSP-Spec have a slightly lower S/N.

Furthermore, we note that the reported Ce differences cannot be explained by differences in the adopted atmospheric parameters since these four studies adopted rather consistent T_{eff} and $\log(g)$, as is shown in Fig. 2. The mean Δ T_{eff} and Δ $\log(g)$ are equal to 106 K and 0.22, respectively, between

---

[3] This value is a good compromise between keeping a high number of stars and good-quality abundances.

[4] Nevertheless, we found a dwarf star (ID=5373254711531881728, $\log(g)$ = 4.21, T_{eff} = 4775.0 K, [M/H] = −0.24 dex, S/N = 81) that appears to be strongly enriched in cerium. ([Ce/Fe] ≥ 2.0 dex, 2.0 being the Ce reference grid high-border value). No clear sign of binarity has been found in the *Gaia* astrometric data for this star, which, moreover, does not belong to the *Gaia* binary catalog. No abundance of other heavy elements has been found in the literature for these stars either.
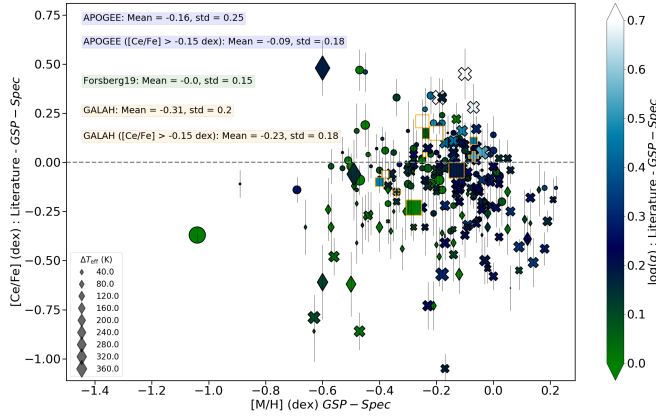
Fig. 2. Comparison between GSP-Spec low-uncertainty sample cerium abundance and literature values as a function of the GSP-Spec metallicity (crosses refer to APOGEE data, circles to F19, and diamonds to GALAH. Squares and plus markers refer to the nine and two stars in common between the strict sample and F19 and APOGEE, respectively). The points are colour-coded with the difference in $\log(g)$, and their size is proportional to differences in T_{eff}. The vertical error bars indicate the uncertainty of GSP-Spec Ce abundance. The mean and the standard deviation of the cerium abundance differences between GSP-Spec and F19 are also given. For APOGEE and GALAH, we provide similar statistics differences for the whole comparison sample and when only their stars with [Ce/Fe] > −0.15 dex are considered. We used calibrated GSP-Spec and APOGEE atmospheric parameters.

GSP-Spec and APOGEE data and 30 K and 0.06 between GSP-Spec and GALAH data[5].

Finally, the comparison between GSP-Spec and F19 allows us to conclude that both studies are on the same reference scale (which is not the case for APOGEE), and that no calibration is required to interpret the GSP-Spec [Ce/Fe].

3. Chemo-kinematics and dynamical properties of selected *Gaia* cerium abundances

In this section, we present the distribution of spatial, kinematical, dynamical, and chemical properties of the low-uncertainty sample defined in the previous section. The computation of the stellar positions (galactocentric Cartesian coordinates X, Y, Z) as well as the galactocentric radius (R) and cylindrical velocities (V_R, V_Z and V_ϕ) is presented in Gaia Collaboration (2023a) and is based on the Bailer-Jones et al. (2021) *Gaia* EDR3 distances. The orbital parameter calculation (eccentricities, actions, apocenters, pericenters, and Z_{max}) is described in Palicio et al. (2023).

3.1. Chemical distribution

We first present in Fig. 3 the Kiel diagram (upper panels) of the low-uncertainty sample stars, colour-coded in stellar counts, metallicity, and cerium abundances (top, central, and bottom panels, respectively). This sample is mainly composed of red giant branch (RGB) and AGB stars with $\log(g) < 3.5$. This results from the fact that the studied cerium line is more easily detected in cool giant stars. Moreover, the stars with a detected Ce line in the low-uncertainty sample are increasingly more metal poor the cooler the giants and the lower their gravity. Cerium abun-

dances were indeed derived for any metallicity including solar in stars located on the RGB, whereas only stars with a metallicity lower than ∼−0.5 dex are present at the top of the AGB. This again results from the difficulty of correctly measuring the Ce line in cool star spectra that become more and more crowded by molecular lines as T_{eff} decreases. This is also illustrated in the right panel of Fig. 3, showing that only the coolest AGB stars ($T_{\mathrm{eff}} \lesssim 3800$ K) with relatively high cerium abundances ([Ce/Fe] $\gtrsim 0.60$ dex) have been measured. Similarly, only Ce-rich stars hotter than $T_{\mathrm{eff}} \gtrsim 4800$ K are detected. These observational biases are discussed in Sect. 4.1. We also remark that there is a lack of stars around $T_{\mathrm{eff}} \sim 4000$ K. This feature is caused by the complexity of the coolest giant spectra. This could lead to some parametrisation issues that were partly fixed through the *KMgiantPar* flag, even if this means rejecting part of these AGB stars (see Recio-Blanco et al. 2023, for more details on this flag).

The lower panels of Fig. 3 present the trend of cerium abundances with metallicity, colour-coded with stellar counts (left bottom panel) and with calcium abundances (right bottom panel). We adopted the calibrated Ca abundances according to Table 4 of Recio-Blanco et al. (2023) below, using the polynomial of degree 4 as a function of $\log(g)$ and a calibration for $\log(g)$ values outside the recommended gravity interval set to those computed for the limiting values. For all the low-uncertainty sample stars, their *CaUpLim* and *CaUncer* flags are equal to zero, and their uncertainties in [Ca/Fe] are smaller than 0.06 dex. Over a metallicity range of 1.5 dex, we found a banana-like shape that can be explained by some detection bias. For example, low-Ce metal-poor stars are poorly represented in our sample because the Ce line becomes too weak to be detected in these stellar atmospheres. Similarly, low Ce abundances are more difficult to derive in crowded metal-rich spectra.

On the other hand, the lower right panel shows that the sample is composed of stars that are more Ca-rich with decreasing metallicity, a consequence of the behaviour of α-elements with [M/H] in the Milky Way. In the most metal-poor regime, there are predominantly Ce-rich stars ([Ce/Fe] $\gtrsim 0.5$ dex) with high calcium abundances ([Ca/Fe] $\gtrsim 0.3$ dex).

We finally note an excess of stars with rather low [Ce/Fe] and [Ca/Fe] abundances around [M/H] = −0.5 dex. As explained in Gaia Collaboration (2023a), these stars are mostly massive and young (see their Fig. 8) and are located in the spiral arms of the Milky Way. This is confirmed by the recent work of Poggio et al. (2022; see their Fig. B.1.). Their sample A is a sub-sample containing the majority of the massive star sample defined in Fig. 8 of Gaia Collaboration (2023a). These stars present very young ages (<500 Myr) and are massive.

There are also some other stars with low [Ce/Fe] and solar [Ca/Fe] that probably belong to the disc because they have similar spatial distribution and kinematics as other disc stars.

3.2. Spatial distribution

We illustrate in Fig. 4 the spatial distribution of the low-uncertainty sample stars. Three maps in the (X, Y) plane are shown in the top panels. These maps are colour-coded by stellar counts, median metallicity, and median [Ce/Fe] (from left to right). The bottom panels of Fig. 4 show the same sample stars in the (R, Z) plane. We first remark that the spatial coverage is quite large (about 7 kpc in X, Y and Z), even though most of the sample is concentrated in the solar neighbourhood. However, it is worth noting that this figure shows (and comparison of it to the Kiel panels of Fig. 2) that the most metal-rich stars have preferentially larger $\log(g)$ are found closer to the Sun, while the most

---

[5] A comparison of GSP-Spec T_{eff} and $\log(g)$ with literature values is commented on in Recio-Blanco et al. (2023).
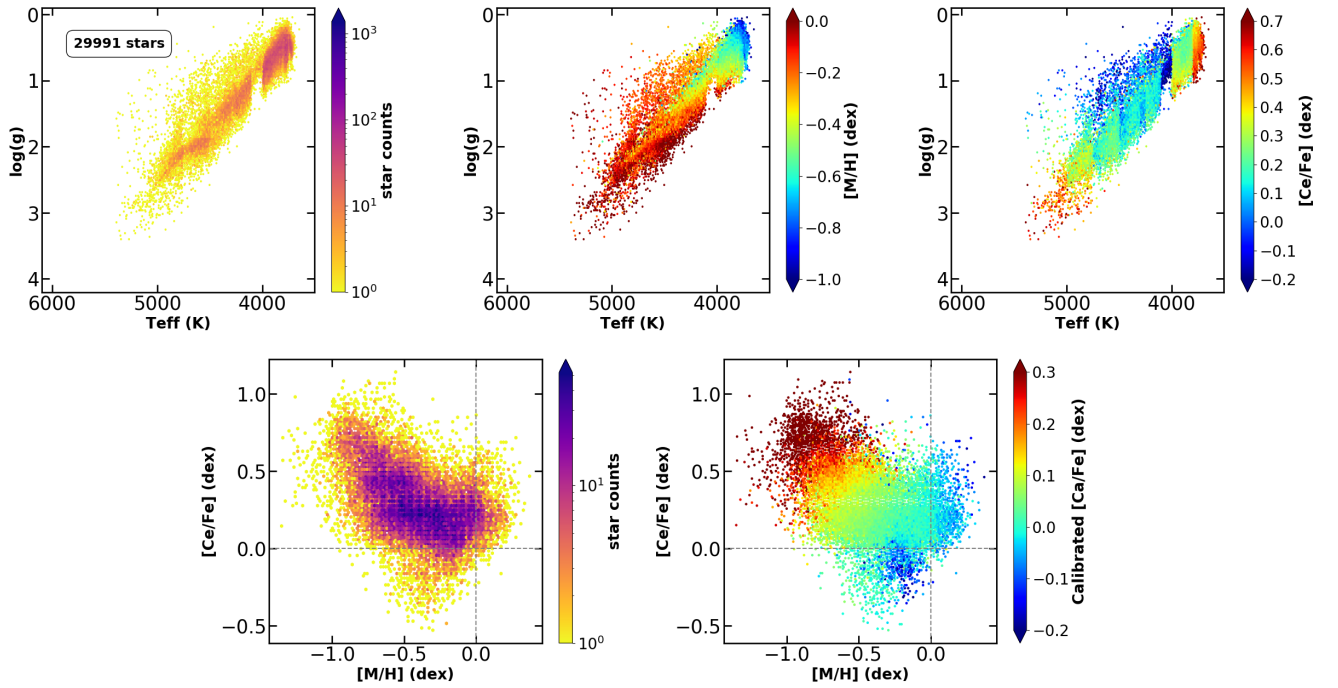
Fig. 3. *Upper panels*: Kiel diagram of the low-uncertainty sample stars colour-coded with stellar counts (*left panel*), medium metallicity per point (*central panel*), and medium cerium abundances (*right panel*). *Lower panels*: [Ce/Fe] vs. [M/H] distribution colour-coded in stellar counts (*left panel*) and median calibrated calcium abundances (*right panel*).
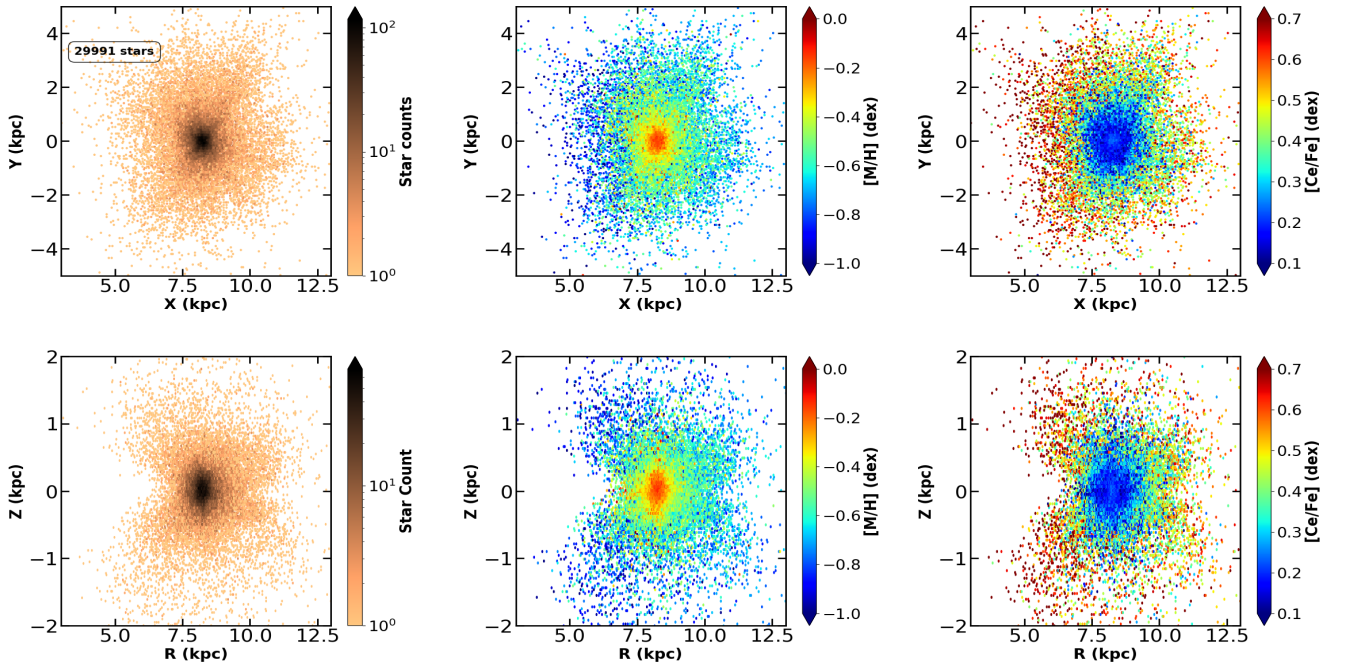

Fig. 4. Galactic distributions of the low-uncertainty sample stars. The *upper panels* show the distributions in Cartesian coordinates (X, Y), colour-coded *from left to right* by stellar counts, median metallicities, and median cerium abundances. The *bottom panels* show the (R, Z) distributions with similar colour-coding as the *top panels*.

metal-poor stars are more likely to be giants and can be seen out to larger distances. This results from some observational biases that are treated in Sect. 4.1

In addition to these possible biases, the closest stars, which are rather more metal rich and more Ce poor than the more distant stars, probably belong to the thin disc as they are mainly concentrated within ±0.5 kpc from the Galactic plane. Moreover,

their Z_{max} is lower than 0.8 kpc for about 90% of them. There could thus nevertheless be a small contribution from thick-disc or halo stars in this sample. On the other hand, stars with higher Ce abundances are found to be more metal poor (see Fig. 3) and are preferentially located outside the solar neighbourhood and/or at larger distances from the Galactic plane. Part of this population probably does not belong to the thin disc because it
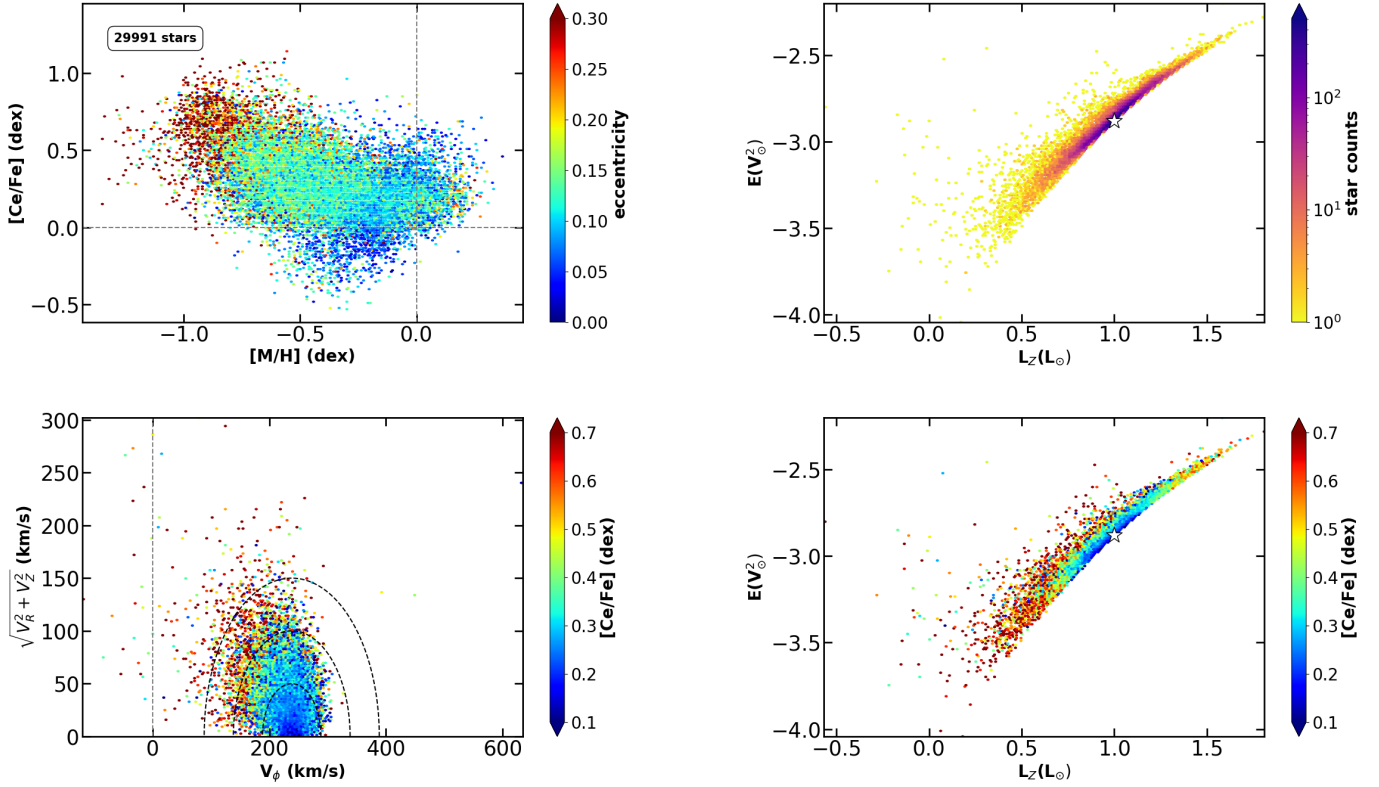
Fig. 5. *Left upper panel*: distribution of cerium vs. metallicity for the low-uncertainty sample stars, colour-coded with the eccentricity of their orbits. *Left lower panel*: Toomre diagram colour-coded with [Ce/Fe]. The circular dashed lines corresponds to $V_{Tot} = 50$, 100 and 150 km s^{-1}. *Right panels*: Energy-angular momentum (E, L_Z) plane colour-coded by density (*top panel*), and medium cerium abundance (*lower panel*). The white star indicates the solar neighbourhood ($L_Z = L_\odot$, $E \approx -2.88V_\odot^2$).

is located at $|Z| > 1$ kpc. This agrees with their metallicity and Ca content (see the bottom right panel of Fig. 3).

3.3. Chemo-kinematics and chemo-dynamics

Based on the kinematical and orbital parameters presented in Palicio et al. (2023), we show in the upper left panel of Fig. 5 the Ce abundances with respect to the metallicity, colour-coded with the median eccentricity of their Galactic orbit. We remark that the stars with higher Ce abundances orbit on more eccentric orbits. This confirms that these stars probably do not belong to the thin disc. In contrast, more metal-rich stars with a Ce abundance are on almost circular orbits with Z_{max} smaller than ~800 pc, which is typical of thin disc stars.

These trends are confirmed by the Toomre diagram of the low-uncertainty sample stars (left bottom panel of Fig. 5) colour-coded by the median [Ce/Fe]. Ce-enriched stars are mostly outside the annulus of 150 km s^{-1}, suggesting that they belong to the Galactic halo and/or thick disk. We can also see that a huge majority of these stars (95.4%) exhibit disc kinematical properties since their total velocity is always lower than ~100 km s^{-1}. This is confirmed by their Z_{max}, which is smaller than 800 pc for ~85% of the low-uncertainty sample. Despite this dominance of the disc population, it is worth noting that a smaller proportion of halo stars, including objects on retrograde orbits, is also present.

Finally, the right panels show the total energy E (rescaled in terms of $V_\odot^2$) with respect to the vertical component of the angular momentum L_Z (fixed as positive in the direction of Galactic rotation), colour-coded in stellar counts (upper panel) and [Ce/Fe] abundances (lower panel). These plots again con-

firm that the large majority of the low-uncertainty sample stars is located inside the Galactic disc, and especially close to the Sun (indicated by the white star in the figure). In addition, lower angular momentum halo stars can be observed. Some of these stars fall into already identified halo substructures such as the Gaia-Enceladus-Sausage (GES; see Helmi et al. 2018; Belokurov et al. 2018; Myeong et al. 2018; Feuillet et al. 2020, 2021) at low $|L_Z|$ and $-2.8V_\odot^2 \lesssim E \lesssim -2.0V_\odot^2$. These stars are discussed in Sect. 5.1 by extending the analysis to the complete sample.

4. Cerium in the Galactic disc

In this section, we discuss the chemical evolution of cerium in the Galactic disc based on these GSP-Spec data. For this purpose, it has to be taken into account that the low-uncertainty sample defined in Sect. 2 could be biased by some selection function effects, for instance, spatial distribution and stellar parameter limitations. In particular, the GSP-Spec cerium line cannot be detected and measured for any combination of stellar atmospheric parameters. Ce abundances are indeed available only for giant stars, as already shown in Fig. 3. Moreover, only the brightest AGB stars located far outside the solar neighbourhood can have a derived [Ce/Fe]. Similarly, we showed that cerium abundances are measured with difficulty in crowded spectra of metal-rich and/or very cool stars. This could favour the detection of Ce-enriched stars, not always representative of the ISM Galactic content, due to the modification of the atmospheric s-element abundances in evolved low-mass stars caused by the internal
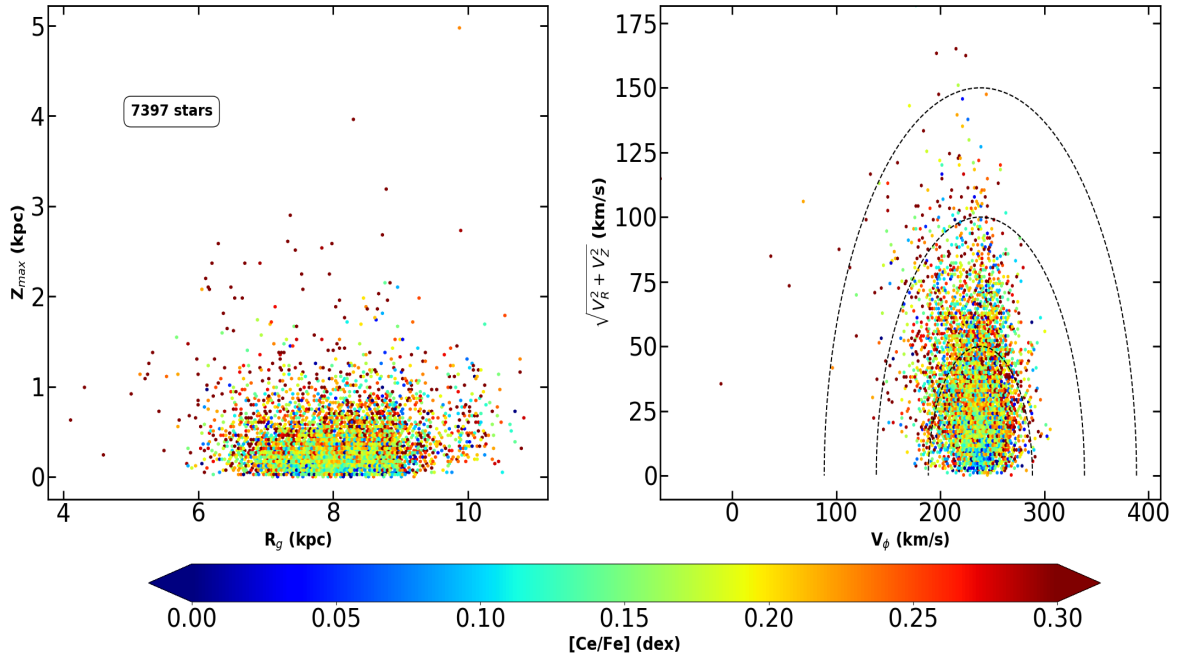
Fig. 6. *Left panel*: galactic distribution in the $(R_g–Z_{max})$ plane of the high-quality sample stars colour-coded with the median cerium abundances per point. *Right panel*: Toomre diagram of the same stars.

production. To take these biases into account, we defined a new stellar subsample (called high-quality sample, hereafter) in order to discuss Galactic Ce gradients and trends. The Galactic evolution of this neutron-capture element is then interpreted based on a chemical evolution model. Finally, we explore the [Ce/Fe] abundances in open clusters by tracing Galactic gradients complementary to field stars.

4.1. High-quality sample of Ce abundances

To consider the most accurate Ce abundances (low uncertainties and best stellar parametrisation) and to avoid detection biases towards more Ce-rich stars, we selected only results for $S/N \geq 300$ and [Ce/Fe] uncertainty ≤ 0.10 dex. Then, since the Ce line is more easily detected in cool stars, we kept only stars with $3800 \leq T_{\mathrm{eff}} \leq 4800$ K (as discussed from Fig. 3 and associated text). On one hand, hotter star spectra have a very weak and almost undetectable Ce line (as already shown in Fig. 1), thus only Ce-rich stars can be measured at these temperatures. On the other hand, the cut at low T_{eff} rejects the coolest AGB stars of the sample, most of them being metal poor and Ce rich (see the top panels of Fig. 3). These stars are probably enriched in Ce due to their internal nucleosynthesis and mixing. Their properties will be discussed in a future article.

Finally, the high-quality sample is composed of 7397 stars mainly located within 1 kpc from the Sun in $X − Y$ coordinates. The left panel of Fig. 6 shows their location in the $(R_g–Z_{max})$ plane. Only a few of them have $|Z_{max}| > 0.7$ kpc ($\sim$10% of the sample). Their Galactic velocities are compatible with a membership to the disc, as can be deduced from the Toomre diagram presented in the right panel of Fig. 6, which shows that $\sim$85% of them have a total velocity lower than $\sim$70 km s^{-1} and a Z_{max} smaller than 700 pc.

4.2. [Ce/Fe] versus [M/H] trends

In order to validate this high-quality sample, we illustrate the [Ce/Fe] trend with respect to metallicity in the top panel
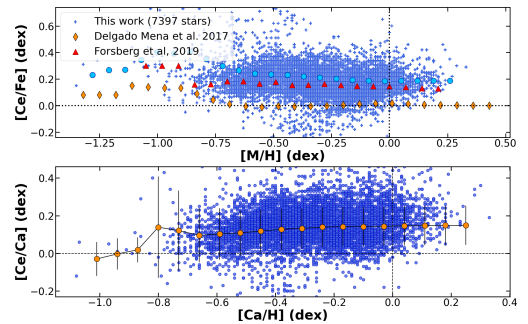

Fig. 7. *Top panel*: cerium and iron abundances ratio for the high-quality sample with respect to the metallicity. Red triangles and orange diamonds are mean [Ce/Fe] ratios for the stars of F19 and Delgado Mena et al. (2017), respectively (computed per bins of 0.07 dex). Sky blue points: the mean of our data per bin of 0.07 dex in [Ca/H]. *Bottom panel*: [Ce/Ca] vs. [M/H]. Orange dots correspond to the mean of the measurements per bin of 0.07 dex, and the error bars correspond to the standard deviation in each bin.

of Fig. 7. We found a rather flat trend at a mean level of [Ce/Fe] $\sim$ 0.2 dex for metallicities varying between $\sim$–0.7 up to $\sim$+0.3 dex. A similar behaviour and mean level of [Ce/Fe] is reported by F19, based on 277 stars (red triangles in Fig. 7, top panel). This flat trend also agrees with Reddy et al. (2006; 178 stars), Battistini & Bensby (2016; 365 stars), and Delgado Mena et al. (2017; orange diamonds in Fig. 7, top panel, 653 stars). These stars have $T_{\mathrm{eff}} > 5300$ K and $S/N > 100$, according to their Sect. 4), although these authors report a lower [Ce/Fe] level ($\sim$+0.0 dex), probably resulting from different calibrations and/or reference scales. Finally, it is worth noting that in the low-metallicity regime ([M/H] $\lesssim −0.8$ dex), the high-quality sample is probably not statistically representative.

The bottom panel of Fig. 7 shows the [Ce/Ca] abundance ratio versus [Ca/H]. Orange dots again illustrate the running mean [Ce/Ca] abundance in bins of 0.07 dex in [Ca/H]. Error

bars are the associated standard deviation for each bin. For values of [Ca/H] higher than ~ -0.7 dex (low statistics blur the trend at lower metallicities), we found a slightly increasing [Ce/Ca] abundance with increasing [Ca/H] (δ[Ce/Ca]/δ[Ca/H] = $0.087^{\pm 0.013}$), similar to the trend of the high-Ia population of Griffith et al. (2021; this population represents their thin-disc low-[Mg/Fe] distribution). It is important to note that Griffith et al. (2021) used Mg abundances from APOGEE DR16 data, while the α-element reference is Ca in our study[6]. This continuous increase in [Ce/Ca] could be the consequence of the later contribution of AGB stars (main producers of s-process elements, such as cerium) in the Galactic chemical evolution history with respect to SN II (producers of α-elements as Ca). Moreover, we point out that we also found a rather flat distribution of the [Ce/Ca] ratio for [Ca/H] > 0.1 dex, whereas Griffith et al. (2021) reported a strong decrease. This is due to the different trend of our Ca and their Mg abundances. Their [Mg/Fe] remains constant for positive metallicities, in contrast to the continuous decrease in our [Ca/Fe], as shown in Fig. 25 of Recio-Blanco et al. (2023). This continuous decrease agrees better with Galactic evolution models that predict a similar decrease in any [α/Fe] ratios with [M/H]. We also note that our [Ce/Ca] is systematically higher than that of Griffith et al. (2021), probably because of the different reference scales that were adopted.

Finally, we emphasize that this Fig. 7 and our conclusions are not modified when the calibrated metallicities proposed by Gaia Collaboration (2023a) are adopted. We therefore decide to not calibrate [M/H] in the following.

4.3. Cerium abundance radial gradients.

The radial Ce abundance gradients of the Galactic disc were computed using a Theil-Sen fit of the high-quality sample trends with respect to i) the radial distance to the Galactic centre R, and ii) the guiding radius (R_g, approximated by the mean of the orbital apocentre and pericentre distances). Errors were computed by adopting a confidence level of 0.95.

First of all, we examined the [Ce/Fe] radial gradients, and flat gradients with respect to R or R_g were found. The corresponding fits are δ[Ce/Fe]/$\delta R = -0.001^{\pm 0.004}$ dex.kpc^{-1} for the Galactic radius, and δ[Ce/Fe]/$\delta R_g = -0.001^{\pm 0.005}$ dex.kpc^{-1} for the Galactic guiding radius.

We therefore find that the ISM [Ce/Fe] content is constant for R_g within 7.5 and 9.5 kpc from the Galactic centre. This flat gradient within the Galactic disc has a smaller slope (although it almost agrees within the error bars) with respect to the gradient in R_g reported by Tautvaišienė et al. (2021), assuming that their mean galactocentric distances are equivalent to our R_g. Considering only their thin-disc stars, they indeed found a radial gradient of 0.015 ± 0.007 dex.kpc^{-1} over a similar range in R_g. We found 32 stars in common between the high-quality sample and Tautvaišienė et al. (2021), with a mean difference in [Ce/Fe] and a standard deviation of -0.25 and 0.16 dex, respectively. The two studies therefore agree well, although they are not on the same reference scale. However, this different scale do not affect the cerium gradient determination. As a consequence, the difference between the two derived gradients might be explained by the smaller number statistics of the Tautvaišienė et al. (2021) study, which relied on only 424 stars (i.e. less than 6% of the GSP-Spec

sample). As a consequence, selection function biases might be more important in this last study.

Secondly, the [Ce/H] radial gradients were derived and were found to be marginally negative: δ[Ce/H]/$\delta R = -0.028^{\pm 0.017}$ dex.kpc^{-1} and δ[Ce/H]/$\delta R_g = -0.051^{\pm 0.007}$ dex.kpc^{-1}. They are fully consistent with the [Ce/H] and [La/H][7] horizontal gradients (δ[Ce/H]/$\delta R = -0.024^{\pm 0.003}$ dex.kpc^{-1} and δ[La/H]/$\delta R = -0.020^{\pm 0.003}$ dex.kpc^{-1}) derived from Cepheids by da Silva et al. (2016) over a wider range of galactocentric distances (4–18 kpc). Our result also agrees with the negative radial metallicity gradients of the disc reported for *Gaia* data by (see Gaia Collaboration 2023a, Sect. 4).

4.4. Cerium abundance vertical gradients

On one hand, the [Ce/Fe] vertical gradient was derived with respect to the absolute distance to the Galactic plane |Z|. A positive trend was found with δ[Ce/Fe]/$\delta Z = 0.122^{\pm 0.016}$ dex.kpc^{-1}. On the other hand, the gradient with respect to the maximum orbital distance to the plane, Z_{max}, provides a rather similar value: δ[Ce/Fe]/$\delta Z_{max} = 0.086^{\pm 0.011}$ dex.kpc^{-1}. These two gradients are not affected when stars located at distances larger than ~ 600 pc from the plane are rejected. An opposite trend was found by Tautvaišienė et al. (2021; -0.034 ± 0.027 dex.kpc^{-1}) for their thin-disc gradient, probably due to the selection function biases we discussed above. Nevertheless, we note that these authors found a positive gradient for La in the thin disc (δ[La/Fe]/$\delta R_g = 0.030^{\pm 0.025}$ dex.kpc^{-1}) in better agreement with our vertical gradient and surprisingly in contrast with their Ce gradient.

Finally, we found decreasing [Ce/H] vertical gradients: δ[Ce/H]/$\delta Z = -0.453 \pm 0.035$ dex.kpc^{-1} and δ[Ce/H]/$\delta Z_{max} = -0.297 \pm 0.021$ dex.kpc^{-1}. These are related to the vertical metallicity gradient that we derived: δ[M/H]/$\delta Z = -0.614 \pm 0.032$ dex.kpc^{-1}.

4.5. Comparison with Galactic evolution models

Spitoni et al. (2023) presented a new chemical evolution model designed to reproduce GSP-Spec [X/Fe] versus [M/H] abundance ratios, where X stands for several α-elements in the solar vicinity. This model is an extension of recent two-infall models (Spitoni et al. 2020, 2021) designed to reproduce APOKASC and APOGEE data assuming that high- and low-α sequence stars are formed by means of two independent episodes of gas infall. However, Gaia Collaboration (2023a) clearly showed a young chemical impoverishment in metallicity and with low [α/Fe] values. In the new model proposed by Spitoni et al. (2023), this population is well traced when the low-α population is generated by two sequential infall episodes. It is worth mentioning that this model is also able to reproduce the star formation history as constrained by previous *Gaia* releases (Bernard 2017; Ruiz-Lara et al. 2020). In conclusion, an original three-infall chemical evolution model for the disc components has been proposed. This three-infall model is also motivated by the recent work of De Cia et al. (2021), who highlighted the recent infalling gas of pristine chemical composition in the interstellar medium. Vincenzo & Kobayashi (2020) showed important signatures of recent metal-poor gas accretion from Milky Way-like simulations in the cosmological framework (0–2 Gyr ago).

---

[6] We adopted Ca instead of Mg as several of the high-quality sample stars lack GSP-Spec magnesium abundances.

[7] La is a second-peak s-process element that shares a similar production history as Ce (see e.g. Prantzos et al. 2018).
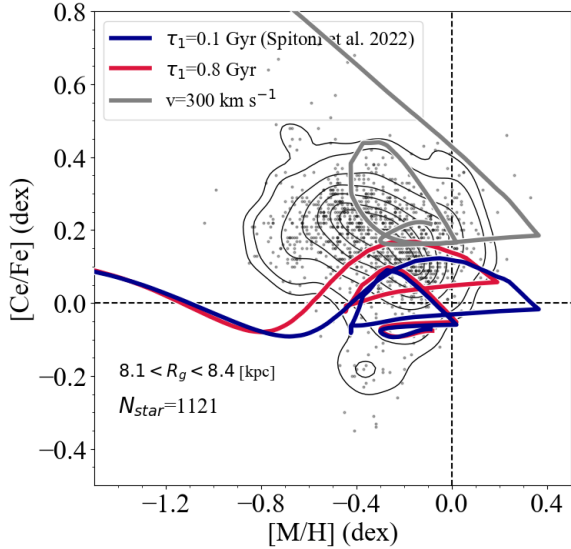
Fig. 8. Model predictions for the chemical evolution of Ce in the [Ce/Fe] vs. [M/H] plane (high-quality sample). The blue line stands for the model assuming the same parameter as in Spitoni et al. (2023, see their Table 2). In this case, the timescale of the gas accretion for the high-α sequence is $\tau_1 = 0.1$ Gyr. The red line shows the case with $\tau_1 = 0.8$ Gyr. The grey line represents the model where the yields of Limongi & Chieffi (2018) for rotating massive stars assuming that all stars rotate with an initial velocity of 300 km s^{-1} have been considered. GSP-Spec stars with guiding radii R_g between 8.1 and 8.4 kpc are indicated with grey points. The contour lines enclose fractions of 0.95, 0.90, 0.75, 0.60, 0.45, 0.30, 0.20, and 0.05 of the total number of observed stars.

We refer to Table 2 of Spitoni et al. (2023) for the values of the adopted model parameters.

In this section, we show predictions of this three-infall model for the chemical evolution of Ce. We recall that Ce is formed from both the s- and r-process channels (Arlandini et al. 1999):

- The most part of the s-process in Ce is synthesised in low-mass AGB stars in the mass range 1.3–3 $M\odot$, and the corresponding yields are taken from Cristallo et al. (2009, 2011).
- The contribution of the s-process from rotating massive stars was also taken into account. First implemented by Cescutti et al. (2013), Cescutti & Chiappini (2014), Cescutti et al. (2015) considering the nucleosynthesis prescriptions of Frischknecht et al. (2012), we included the yields of Frischknecht et al. (2016), as indicated in Table 3 of Rizzuti et al. (2019). We also tested the yields produced by rotating massive stars as proposed by Limongi & Chieffi (2018).
- The Ce yields produced by the r-process have been computed scaling the Eu yields according to the abundance ratios observed in r-process-rich stars (Sneden et al. 2008). For Eu nucleosynthesis, we included the production of Eu from neutron star mergers (NSM). Following the prescriptions of Matteucci et al. (2014) and Cescutti et al. (2015), the value of the NSM yield is 2×10^{-6} $M\odot$ and the time delay due to the coalescence of the two neutron stars is equal to 1 Myr. We refer to Sect. 3.2.2 of Grisoni et al. (2020) for further details.

In Fig. 8 we compare our model predictions for [Ce/Fe] versus [M/H] abundance ratio in the solar vicinity with the high-quality sample stars defined above. We also considered only

stars with guiding radii $R_g \in [8.1, 8.4]$ kpc, consistent with the Spitoni et al. (2023) stellar samples.

First, we recall that Grisoni et al. (2020) followed the evolution of the Galactic thick and thin discs with a parallel approach (Grisoni et al. 2017) by means of two distinct infall episodes evolving separately (i.e. two distinct chemical evolution tracks in the [Ce/Fe] versus [Fe/H] space). Our model predictions agree with the findings reported in Fig. 2 of Grisoni et al. (2020) for the high-α sequence, although less Ce-rich stars are predicted when compared to the GSP-Spec observations (see discussion below). On the other hand, for low-α stars, the chemical dilution from gas infall episodes (which create two loop features in the [Ce/Fe] versus [M/H] ratio plane) is absent in the Grisoni et al. (2020) prediction.

The most recent dilution event, which started ~2.7 Gyr ago, has the main effect of impoverishing the metallicity of the younger stellar populations (see Gaia Collaboration 2023a) and also allows us to predict the young population at subsolar [Ce/Fe] and [M/H] values seen in Fig. 8.

In addition, we tested the effects on the model of different values for the timescales of gas accretion in the high-α sequence assuming 0.1 Gyr (as in Spitoni et al. 2023) and 0.8 Gyr. We note that a longer timescale helps to better reproduce the data by predicting higher [Ce/Fe] values, as observed. Different nucleosynthesis prescriptions to improve the agreement between the three-infall model and the observed [Ce/Fe] even more, especially some stars with higher [Ce/Fe] values, will be considered in a future work. But we can already conclude that the *three-infall* chemical evolution model well reproduces the observed [Ce/Fe] abundances if a longer results time-scale for the last gas accretion is considered.

Finally, we stress that our results also agree with the model predictions of Prantzos et al. (2018), who considered the yields of massive stars of Limongi & Chieffi (2018) weighted by a metallicity-dependent function of the rotational velocities. In Fig. 8 we also show the results for an extreme case. We assumed the same parameter as in Spitoni et al. (2023), but considering the contribution of rotating massive stars of Limongi & Chieffi (2018), where all stars rotate with the highest initial velocity of 300 km s^{-1}. We are aware that this choice for all stars formed at all metallicities is not physically motivated. However, Fig. 8 shows that a larger contribution of the highest velocity stars could improve the agreement with the data presented in this work. Nevertheless, as shown in Rizzuti et al. (2019), this extreme nucleosynthesis prescription overproduces the ratio of [Ba/Fe] and [Sr/Fe] abundance ratios.

4.6. Cerium in open clusters

To trace the Ce content in the Galactic disc, we also searched for stars belonging to Galactic open clusters (OC). Since rather few OC members were found within the high-quality sample, we adopted the low-uncertainty sample. To select the OC members, we proceeded as in Gaia Collaboration (2023a) by adopting OC properties and, in particular, ages, from Cantat-Gaudin et al. (2020), Castro-Ginard et al. (2022) and Tarricq et al. (2021) These parameters were derived from stars with a membership probability ≥0.7. The adopted Galactocentric distances for the clusters are those of Gaia Collaboration (2023a). We found 82 stars with [Ce/Fe] estimates belonging to 53 different OCs. Thirty-six of these OCs have only one member in our sample, 12 OCs have two members, and 5 OCs have three or more members. Table B.1 contains the mean [M/H], [Ce/Fe], [Ca/Fe], and number of stars for our 53 open clusters.
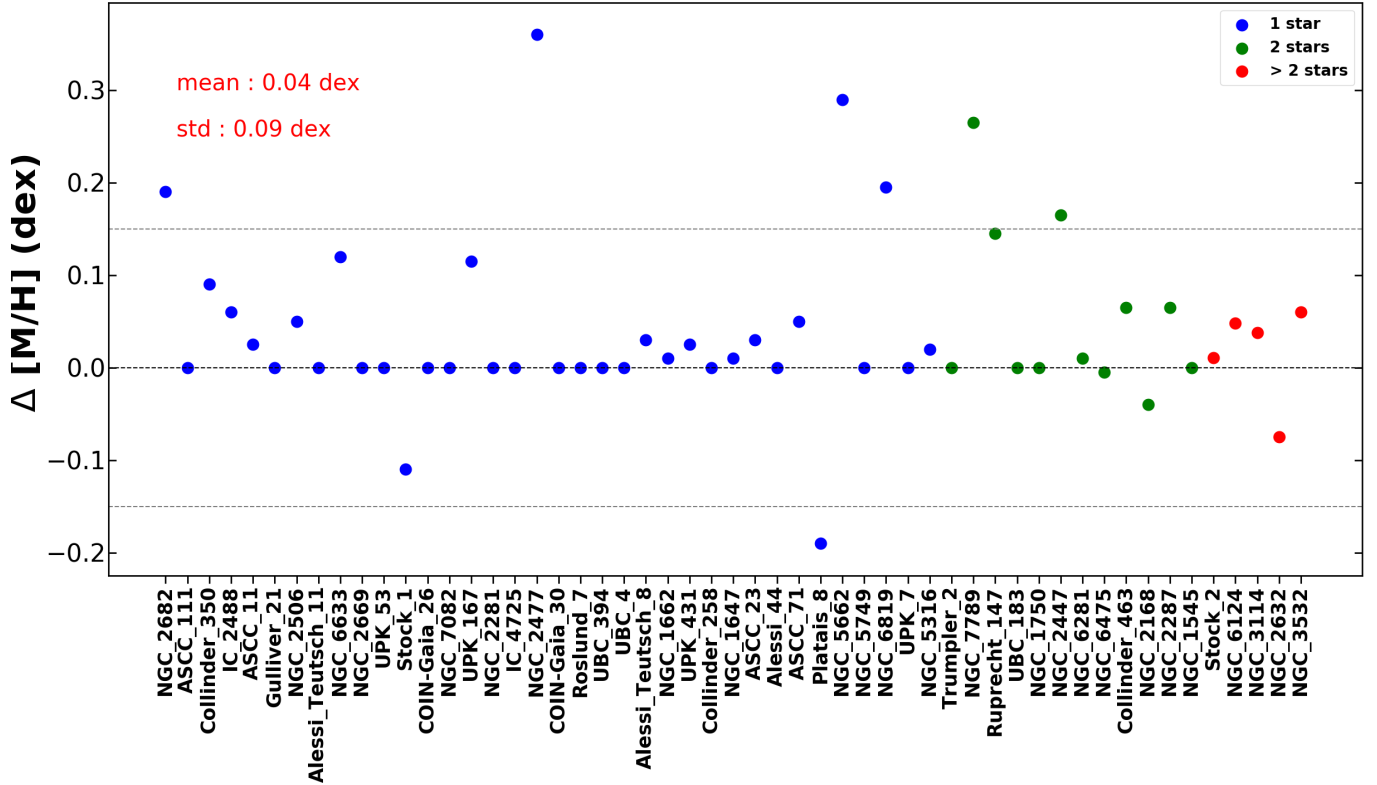
Fig. 9. Difference between literature and GSP-Spec open cluster metallicities (computed as the mean [M/H] of their member) for OC with at least one cerium abundance. Blue, green, and red points indicate the number of stars belonging to each OC (one, two, or more than two members, respectively). The two horizontal lines at ±0.15 dex indicate the OC with good metallicities that are kept for further analysis.

First, the mean metallicity and associated standard deviation for each cluster were derived. Figure 9 compares the GSP-Specmean metallicities for each of them with that of the above-mentioned catalogues. Since these mean [M/H] were estimated from the stars with a Ce abundance, this OC sample is biased by the Ce line detection: for instance, there is a lack of metal-rich clusters. In any case, an excellent agreement is found, with a mean metallicity difference of 0.04 dex and a standard deviation of 0.09 dex, which again confirms the high quality of the GSP-Spec chemical analysis. The metallicity of only three open clusters differs by more than 0.2 dex with respect to the reference value, two of which have only one member (their metallicity difference is around 0.3 dex). In the following, we have kept only the 46 OC with a [M/H] difference with respect to the literature within ±0.15 dex. These good metallicities should be associated with our best derived [Ce/Fe]. We also note that the global accuracy in [M/H] shown in Fig. 9 was very slightly improved when we applied the calibration in metallicity proposed in Table 3 of Recio-Blanco et al. (2023), but the precision remained the same.

We therefore decided to calibrate these metallicities no longer. Fig. 10 compares the GSP-Spec [Ce/M] values with OC literature measurements: Maiorca et al. (2011; red circles), Reddy et al. (2012; green circle), Casamiquela et al. (2021; purples circles), and Sales-Silva et al. (2022; blue circles). The differences between these literature studies and GSP-Spec cerium abundances are Δ[Ce/Fe] = 0.07±0.00, −0.19±0.0, −0.11±0.21, and −0.17±0.13, respectively. We remark that we found a relatively good agreement for our cerium abundances, even though the reference level of Reddy et al. (2012) and Sales-Silva et al. (2022) seems to be different than ours. This last work is indeed on the same scale as the APOGEE DR16 data (they found

a mean difference between their [Ce/H] values and that of APOGEE DR16 of 0.05±0.16). We note that the reference scale of Maiorca et al. (2011) is close to ours, but the difference of 0.07 dex between GSP-Spec data and that of Maiorca et al. (2011) could be explained by the different solar abundances they adopted. They found super-solar abundances of Ce (and elements mainly produced by s- process, e.g., Y, Zr, and La) for their younger OC (with age < 1.5 Gyr).

We illustrate the behaviour of these OC mean [Ce/Fe] abundances in Fig. 11. The left panel shows [Ce/Fe] versus [M/H] colour-coded with the cluster ages. We first remark that older OCs appear to be more enriched in Ce than younger OCs, in contrast to what was found in Sales-Silva et al. (2022). This might be caused by the GSP-Spec biases that are induced when the Ce lines were analysed. This analysis indeed favours the selection of Ce-enriched cool stars in the low-uncertainty sample, as we showed in Fig. 3. When only stars from the high-quality sample are selected (20 stars belonging to 14 OCs), the relation we found between [Ce/Fe] and age is unaffected. Removing AGB stars or stars whose $vbroad$ < 9 km s^{-1} (43 stars) does not affect the relation we found either. Nevertheless, young stars may be affected by chromospheric activity (Spina et al. 2020). We found no sign of chromospheric activity for these stars according to *Gaia* DR3 data ($activityindex\_espcs$ in $gaiadr3.astrophysical\_parameters$), however.

The central panel presents the OC mean [Ce/Fe] abundances with respect to their guiding radius colour-coded with age. Over a guiding radius varying between ~7.2 kpc and 10.5 kpc, we found a radial gradient with a very small slope: δ[Ce/Fe]$/\delta R_g$ = 0.05$^{±0.09}$ dex.kpc^{-1}. We highlight that this value agrees (within the error bar) with the flat gradient reported in Sect. 4.3 from
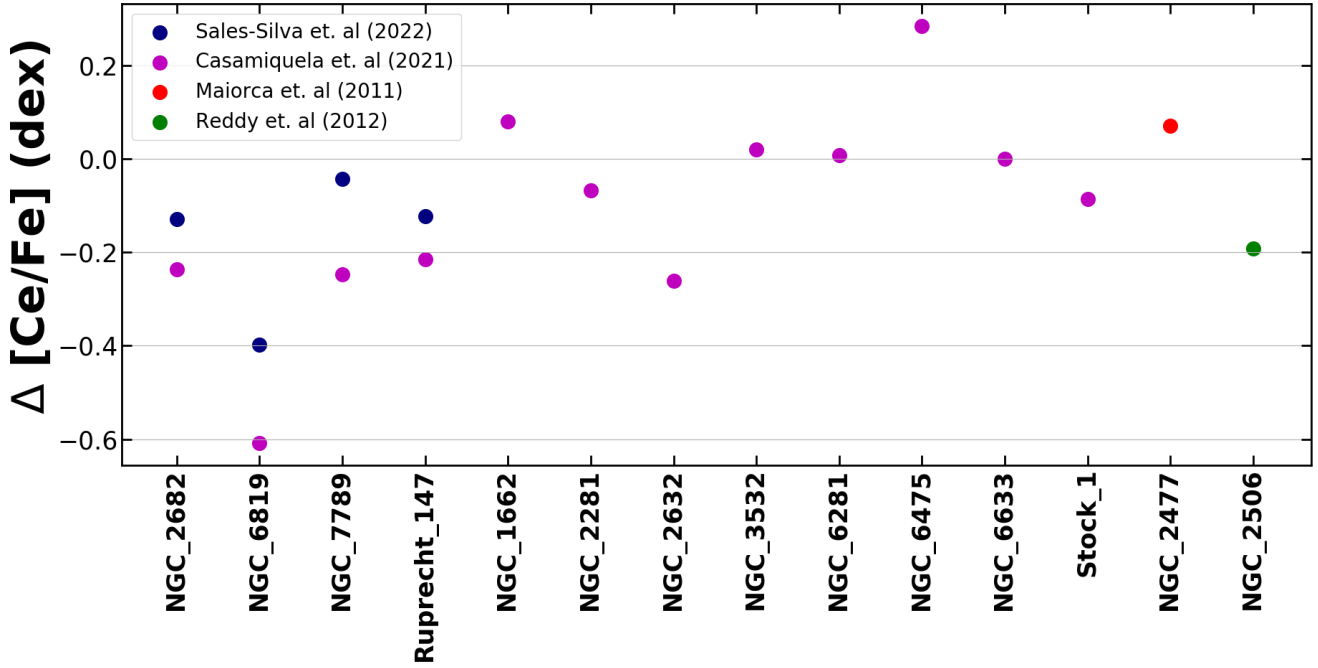
Fig. 10. Difference between literature (blue circles are OC from Sales-Silva et al. 2022, purple circles from Casamiquela et al. 2021, red circles from Maiorca et al. 2011, and green circles from Reddy et al. 2012) and GSP-Spec open cluster [Ce/M] (computed as the mean [Ce/Fe] of their member) for OC with at least one cerium abundance.
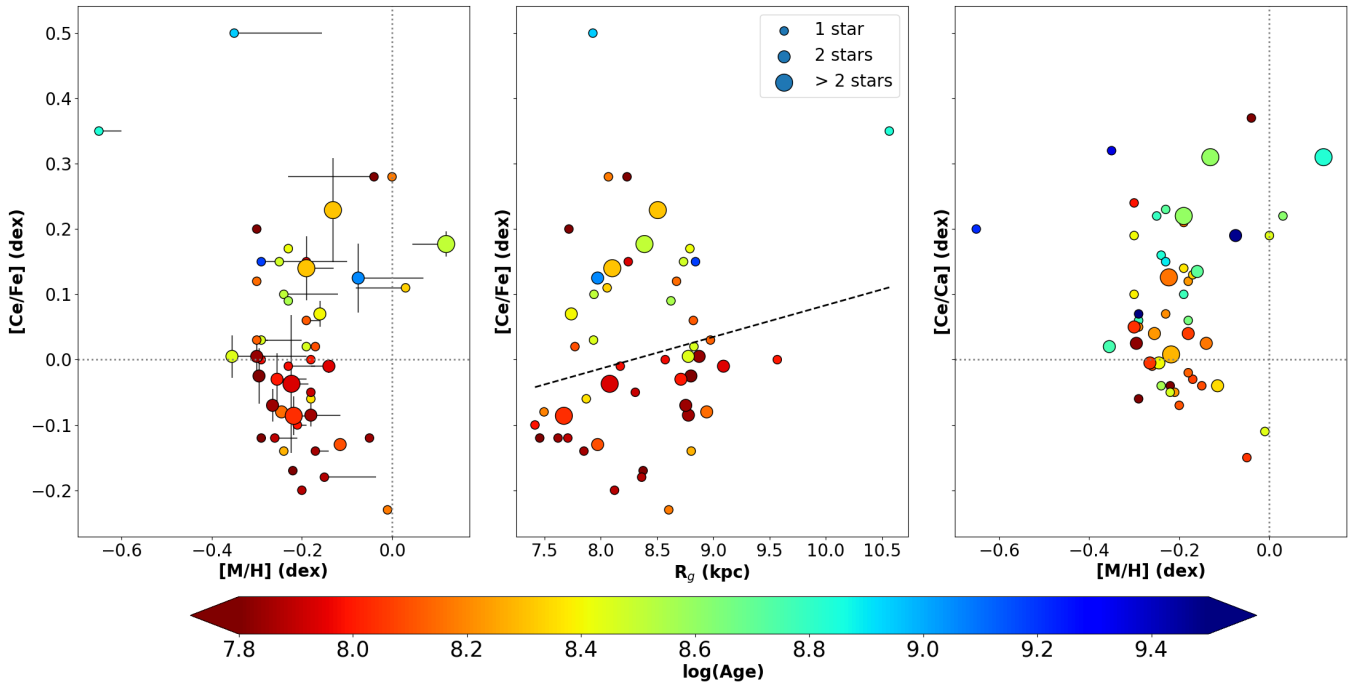
Fig. 11. *Left panel*: [Ce/Fe] vs. [M/H] colour-coded with the OC ages. Each [Ce/Fe] and [M/H] value is the mean of all the OC members. Vertical error bars are the mean dispersion in cerium abundances (star-to-star scatter), and the horizontal lines link the GSP-Spec [M/H] to the reference values. *Central panel*: [Ce/Fe] abundances with respect to the guiding radius colour-coded with age. The dashed line illustrates the derived radial gradient. *Left panel*: [Ce/Ca] ratio with respect to the metallicity colour-coded with the age.

the analysis of field disc stars. We note that removing the most distant cluster does not change the OC gradient significantly (δ[Ce/Fe]$/\delta R_g = 0.00^{\pm0.07}$ dex.kpc^{-1}). As a comparison, Sales-Silva et al. (2022) reported an increasing gradient (δ[Ce/Fe]$/\delta R = 0.014^{\pm0.007}$ dex.kpc^{-1}) over a wider range of R ($\sim$6–15 kpc), which is compatible within the error bars with

our gradient. Finally, our OC radial gradient considering [Ce/H] (δ[Ce/H]$/\delta R_g = -0.01^{\pm0.15}$ dex.kpc^{-1}) is compatible within the error bars with that of Sales-Silva et al. (2022), δ[Ce/H]$/\delta R_g = -0.070^{\pm0.007}$ dex.kpc^{-1}.

Finally, the right panel shows the [Ce/Ca] ratio as a function of metallicity colour-coded with age. No clear trend between

[Ce/Ca] versus [M/H] is seen because of the large scatter. The youngest OC seem to present lower [Ce/Ca] values, which contradicts with what found in Sales-Silva et al. (2022), for instance. To conclude, a further investigation on the biases of our young open clusters could be useful to understand the behaviour we obtained.

5. Cerium in the Galactic halo

As already mentioned in Sect. 3, some GSP-Spec stars with cerium abundances belong to the Galactic halo. We explore the properties of some of them below.

5.1. Cerium in accreted stars

Gaia stellar orbits and kinematics have unveiled the considerable proportion of merger debris in the halo (e.g. Helmi et al. 2018, and references therein), now mixed up with in situ formed objects. As already mentioned above, a small fraction of the low-uncertainty sample stars has the chemo-kinematical and dynamical characteristics of halo stars. Gaia Collaboration (2023a) have explored the *Gaia* DR3 chemical diagnostics of accretion by analysing the metallicity and [α/Fe] characteristics of stars in several overdensities in the ($E - L_Z$) diagram. To complement this first study, we explored the cerium content of these external systems.

In order to search for accreted stars with derived cerium abundances and to increase the statistics, we adopted the complete sample and rejected all stars for which the *KMgiantPar* flag was equal to unity and gof > −3.80 to avoid any parametrisation issue.

Then, after cross-matching with the sample of stars in halo dynamical overdensities presented in Gaia Collaboration (2023a), we found a total of 17 candidate stars with GSP-Spec Ce abundances, two, six, and nine of which lie within the Thamnos (Koppelman et al. 2019; Helmi 2020), the Helmi Stream (Helmi et al. 1999), and the Gaia-Enceladus-Sausage (GES, Helmi et al. 2018; Belokurov et al. 2018; Myeong et al. 2018; Feuillet et al. 2020, 2021) substructures, respectively. Only one of them is found within the low-uncertainty sample (*Gaia* DR3 1294315577499064576 in Thamnos), the others have larger [Ce/Fe] uncertainties, as expected for these fainter objects. We also verified that none of these candidate stars is affected by the observational biases discussed above, which might favour the detection of Ce-enriched stars.

Two of these 17 candidates from the Helmi Stream have already published chemical abundances from the literature, and their accreted nature has already been reported. Sheffield et al. (2012) provided very similar atmospheric parameters for *Gaia* DR3 816615227344979328 to the GSP-Spec ones with differences in T_{eff}, log(g), and [M/H] of 16 K, 0.08, and 0.17 dex, respectively. They confirmed its accreted nature through radial velocities combined with chemical diagnostics (this star has a lower [Ti/Fe] abundance ratio than disc stars). We also have an excellent agreement for the atmospheric parameters of *Gaia* DR3 1275876252107941888: the highest ΔT_{eff}, log(g), and [M/H] is 100 K, 0.3, and 0.10 dex, respectively, with respect to Burris et al. (2000), Ishigaki et al. (2013), Mishenina & Kovtyukh (2001). Our cerium abundance ([Ce/Fe] = 0.27±0.15 dex) is also fully compatible (within the error bars) with that of Mishenina & Kovtyukh (2001; [Ce/Fe] = 0.16 dex) and with other already published s-elements abundances such as barium (Ba, Z = 56) and lanthanum (La, Z = 57) reported by Burris et al. (2000; [Ba/Fe] = 0.08,
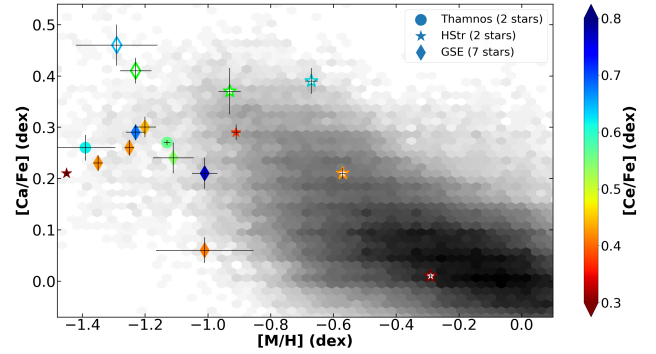

Fig. 12. [Ca/Fe] vs. [M/H] colour-coded with [Ce/Fe] abundances for the identified candidate accreted stars. Circles, stars, and diamonds represent stars belonging to Thamnos, the Helmi Stream, and GSE, respectively. The filled symbols refer to the stars that were selected as good member candidates because of their lower [Ca/Fe], and the empty symbols are the rejected candidates. The density plot in the background are stars from the solar neighbourhood (see text for more details).

[La/Fe] = 0.15 dex) and Ishigaki et al. (2013; [La/Fe] = 0.25). Moreover, Gull et al. (2021) recently identified this star as belonging to the Helmi Stream and classified it as being moderately r-process enhanced.

To chemically confirm the accreted nature of the other 15 stars in our sample, we used the *Gaia* [Ca/Fe] diagnostic, as already performed in Gaia Collaboration (2023a) using the [α/Fe] ratio. Figure 12 presents the 17 candidate stars in the ([Ca/Fe] – [M/H]) plane, colour-coded with [Ce/Fe] abundances. For comparison purposes, the background density plot illustrates a selection of high-quality calcium abundances in the solar cylinder, as defined in Sect. 7 of Gaia Collaboration (2023a). The typical uncertainties in [Ca/Fe] of htese comparison stars are lower than 0.05 dex. This figure shows that 11 of the candidate stars are metal poor ([M/H] < −0.9 dex) and have low [Ca/Fe] ([Ca/Fe] < 0.3 dex) with respect to the standard halo values, as expected for stars that formed in satellite systems. The upper [M/H] and [Ca/Fe] boundaries of our selection are defined by the Helmi Stream star *Gaia* DR3 816615227344979328, which has a confirmed accreted nature in the literature. Table 3 presents the atmospheric parameters and [Ca/Fe] and [Ce/Fe] abundances of our finally selected 11 accreted stars.

Finally, based on this sample of accreted stars, we computed the mean and standard deviation of [M/H], [Ca/Fe], and [Ce/Fe] for each system (see Table 3). For this sample (although based on low-statistics numbers) and within the error bars, the three accreted systems have a rather similar mean metallicity and extremely close mean [Ca/Fe] values. Moreover, Thamnos and GSE appear to have rather similar [Ce/Fe] values, and thus close values of [Ce/Ca] ratios around ∼0.3 dex, which might suggest a rather similar chemical evolution history. In contrast, the Helmi Stream appears to be less enriched in cerium, and its [Ce/Ca] ratio is found to be much lower (∼0.07 dex) than for the other two systems. There are very few previous studies on s-process abundances in these accreted systems. On one hand, Aguado et al. (2021) reported a mean barium abundance for GSE lower than our [Ce/Fe] abundance by about 0.7 dex. On the other hand, Matsuno et al. (2021) found some GSE stars enhanced in Ba and La, in agreement with our cerium abundances (with abundances varying from −0.2 to 1.1 dex and mean [Ba/Fe] and [La/Fe] close to 0.4 and 0.2 dex).

Finally, Recio-Blanco et al. (2021), who analysed Y and Eu abundances on Milky Way satellite galaxies, halo stars,

Table 3. S/N, T_{eff}, $\log(g)$, [M/H], [Ca/Fe], and [Ce/Fe] (and their associated uncertainties) for the 11 accreted stars.

Gaia DR3 Id	S/N	T_{eff} (K)	$\log(g)$	[M/H] (dex)	[Ca/Fe] (dex)	[Ce/Fe] (dex)
Thamnos				**−1.26 ± 0.13**	**0.26 ± 0.01**	**0.59 ± 0.03**
1294315577499064576	657	4309	1.09	−1.13 ± 0.01	0.27 ± 0.01	0.56 ± 0.08
6423592399737133184	102	4180	0.53	−1.39 ± 0.09	0.26 ± 0.02	0.62 ± 0.22
Helmi Stream				**−1.18 ± 0.27**	**0.25 ± 0.04**	**0.32 ± 0.05**
8166152273449793281	174	3916	0.68	−0.91 ± 0.02	0.29 ± 0.02	0.37 ± 0.17
1275876252107941888	410	4391	0.70	−1.45 ± 0.01	0.21 ± 0.01	0.27 ± 0.15
Gaia-Sausage-Enceladus				**−1.16 ± 0.12**	**0.28 ± 0.08**	**0.53 ± 0.13**
4454379718774068736	221	4432	0.68	−1.35 ± 0.01	0.23 ± 0.02	0.42 ± 0.18
4231500087527853696	214	4314	0.80	−1.25 ± 0.01	0.26 ± 0.01	0.42 ± 0.14
810961091879119616	93	4319	0.94	−1.01 ± 0.04	0.21 ± 0.03	0.77 ± 0.21
2744053785077163264	197	4141	0.76	−1.01 ± 0.15	0.06 ± 0.02	0.41 ± 0.19
3232875420468258432	97	4250	1.50	−1.11 ± 0.07	0.24 ±0.03	0.54 ± 0.17
921352299825726208	89	4126	0.66	−1.20 ± 0.04	0.30 ± 0.02	0.44 ± 0.21
614044052605639936	195	4263	0.79	−1.23 ± 0.03	0.29 ± 0.02	0.68 ± 0.19

Notes. For these three accreted systems, we also report the mean and standard deviation of their chemical abundances in boldface.

and globular clusters, showed that the abundances of another s-element [Y/Fe] in low-mass satellites could be slightly lower than in higher-mass satellites in the intermediate-metallicity regime. When a similar behaviour is assumed for Ce, our lower [Ce/Fe] abundances for the Helmi Stream stars could suggest a lower mass of the parent system of this substructure with respect to the other two. It is interesting to point out that, indeed, Koppelman et al. (2019) provided a mass estimate for the Helmi Stream progenitor of about $10^8\,M_\odot$, while the GES mass estimate from simulations would be six times higher (Helmi 2020).

5.2. Globular clusters: M 4 is Ce enriched

We also searched for cerium abundances in stars belonging to Galactic globular clusters (GC). We followed the same procedure as in Gaia Collaboration (2023a). First, we cross-matched the Harris catalogue (Harris 1996) with GSP-Spec data (complete sample) using a maximum separation in the sky of 0.5 degrees. Then, we rejected all potential GC members whose radial velocity departed by more than 20 km s^{-1} from the median value of each GC.

By this method, we found two stars belonging to M 4 (NGC 6121: *Gaia* DR3 6045464990827780608 and 6045463719528135808), and we added two others (6045464166204745344 and 6045490623204749824) found in Yong et al. (2008), who also studied the two first stars. For these four stars, we confirmed that their proper motions agree well with that of M 4, and we found a mean metallicity of −1.20 dex (and a standard 0.08 dex). This mean metallicity is fully compatible with the works of Carretta et al. (2009) and Yong et al. (2008), with differences in metallicity smaller than 0.10 dex, showing the excellent parametrisation of GSP-Spec for these stars. GSP-Spec T_{eff} and $\log(g)$ values of these four stars are also fully compatible with that of Yong et al. (2008). The mean and standard deviation of the differences between the GSP-Spec and Yong et al. (2008) values are 1±45 K and −0.08±0.08, respectively.

GSP-Spec [Ce/Fe] abundances also fully agree with those of Yong et al. (2008) with a mean difference of −0.05 dex, in the sense GSP-Spec minus Yong et al. (2008), and a standard deviation of 0.11 dex.

As a consequence, we found a mean [Ce/Fe] abundance ratio for M 4 equal to 0.46±0.07 dex. This value fully agrees with that found by Yong et al. (2008) for their 11 members ([Ce/Fe] = 0.50±0.10 dex). We note that Yong et al. (2008) also found an enhancement in s-process elements (Ce, Ba, and Pb) in M 4 with respect to M 5, a globular cluster whose s- and r-elements content is similar to that of halo field stars. This could reveal that the contributing sources of the s-process differ between these two globular clusters and may suggest that M 4 could have had a different chemical origin and evolution than M 5 and other halo stars. We note that our M 4 mean metallicity and [Ce/Fe] abundance are similar to those of Gaia Sausage-Enceladus. The mean [Ca/Fe] value is also similar (0.28 dex).

Finally, our [Ce/Fe] is also fully compatible (within the error bars) with other s-process element abundances reported by Brown & Wallerstein (1992) from the analysis of three stars ([Ba/Fe] = 0.57 dex and [La/Fe] = 0.43 dex). In summary, our work therefore confirms the enrichment of M4 in s-process elements with respect to iron.

6. Conclusions

The aim of this paper was to explore the cerium content in the Milky Way disc based on the *Gaia* GSP-Spec derived chemical abundances. We first validated the LTE GSP-Spec cerium abundances with GALAH DR3, APOGEE DR17, and Forsberg et al. (2019) data. We found a good global agreement, even though GALAH and APOGEE do not seem to be on the same scale as GSP-Spec and F19.

We then selected good-quality samples of GSP-Spec cerium abundances using different flag combinations. The general Galactic properties of the selected stars were discussed. We found that a majority of these stars are located within ~1 kpc from the Sun, and that the sample is only composed of giant stars. They belong mainly to the disc as more than 95% of them have a rather low total velocity in the Toomre diagram and a Z_{max} lower than 800 pc. Nevertheless, our sample also contained some metal-poor and cerium-rich stars belonging to the halo, as can be concluded from their velocity, eccentricity, calcium abundances, and their spatial distribution. We also found a young cerium-poor population of stars, as already mentioned in Gaia Collaboration (2023a).

We studied the chemical evolution of cerium in the Galactic disc. For this purpose, we selected a high-quality sample of stars within the parameter range defined by the most sensitive detection degree of the Ce line we used, and excluding cool AGB stars that might be polluted by internal *s*-element production. Based on these different samples, our main results are listed below.

- The radial and vertical gradients of [Ce/Fe] and [Ce/H] in the disc were estimated. We found a flat radial gradient in [Ce/Fe] by adopting both the galactocentric radius and the guiding radius, in agreement with previous findings. The radial gradient in [Ce/H] is found to be strongly negative, consistent with the radial gradient in metallicity. We also found a strong positive vertical gradient in [Ce/Fe] and a negative vertical gradient in [Ce/H]. Moreover, we found a slightly increasing [Ce/Ca] versus [Ca/H] up to [Ca/H] < −0.1 dex, showing the later contribution of AGB stars in the Galactic chemical evolution with respect to supernovae II, which are the main producers of *s*-process and *α*-elements, respectively.
- Our data can be well reproduced by a new three-infall Galactic chemical evolution model (see Spitoni et al. 2023), in which a timescale for the last gas accretion of about 0.8 Gyr is favoured.
- Eighty-two stars with Ce abundances belonging to 53 different OCs have been identified. The derived OC GSP-Spec mean metallicities estimated from stars with Ce abundances agree excellently with the literature metallicities. The relations between OC mean [Ce/Fe], metallicities, and ages were discussed. The derived OC radial gradient in [Ce/Fe] is compatible with the one derived from field stars (within the error bars). A large proportion of our OCs are very young (<1 Gyr) and show a large dispersion in cerium abundances.

We then explored the Ce content in the Galactic halo. Our results are again listed below.

- The mean [Ce/Fe] abundance ratio in the M 4 globular cluster was estimated based on the identification of four of its members. This cluster is found to be enriched in Ce with respect to iron.
- The cerium abundances in three accreted substructures of the Galactic halo (Helmi Stream, Thamnos, and GSE) were then discussed. Two of the GSP-Spec Helmi Stream stars with derived [Ce/Fe] were already known in the literature. Their atmospheric parameters as well as their cerium abundance are fully compatible with that derived by GSP-Spec. Our sample allowed us to estimate the mean [Ce/Fe] content in these accreted systems. We found that the Helmi Stream could be slightly underabundant in cerium compared to the two other systems.

All these results confirm the excellent quality of the *Gaia* data and of the GSP-Spec physico-chemical parametrisation. This study will be extended to the two other *s*-element abundances estimated by GSP-Spec (Nd and Zr), in combination with the analysis of Ce-rich AGB stars identified in this work.

References

Abdurro'uf, N., Accetta, K., Aerts, C., et al. 2022, ApJS, 259, 35
Aguado, D. S., Belokurov, V., Myeong, G. C., et al. 2021, ApJ, 908, L8
Arlandini, C., Käppeler, F., Wisshak, K., et al. 1999, ApJ, 525, 886
Bailer-Jones, C. A. L., Rybizki, J., Fouesneau, M., Demleitner, M., & Andrae, R. 2021, AJ, 161, 147
Battistini, C., & Bensby, T. 2016, A&A, 586, A49
Belokurov, V., Erkal, D., Evans, N. W., Koposov, S. E., & Deason, A. J. 2018, MNRAS, 478, 611
Bernard, E. J., 2017, in SF2A-2017: Proceedings of the Annual meeting of the French Society of Astronomy and Astrophysics, eds. C. Reylé, P. Di Matteo, F. Herpin, et al.
Bijaoui, A. 2012, in Seventh Conference on Astronomical Data Analysis, eds. J. L. Starck, & C. Surace, 2
Birch, K. P., & Downs, M. J. 1994, Metrologia, 31, 315
Bisterzo, S., Gallino, R., Straniero, O., Cristallo, S., & Käppeler, F. 2011, MNRAS, 418, 284
Bisterzo, S., Gallino, R., Käppeler, F., et al. 2015, MNRAS, 449, 506
Bisterzo, S., Travaglio, C., Wiescher, M., et al. 2016, J. Phys. Conf. Ser., 665, 012023
Brown, J. A., & Wallerstein, G. 1992, AJ, 104, 1818
Buder, S., Sharma, S., Kos, J., et al. 2021, MNRAS, 506, 150
Burbidge, E. M., Burbidge, G. R., Fowler, W. A., & Hoyle, F. 1957, Rev. Mod. Phys., 29, 547
Burris, D. L., Pilachowski, C. A., Armandroff, T. E., et al. 2000, ApJ, 544, 302
Busso, M., Gallino, R., & Wasserburg, G. J. 1999, ARA&A, 37, 239
Cantat-Gaudin, T., Anders, F., Castro-Ginard, A., et al. 2020, A&A, 640, A1
Carretta, E., Bragaglia, A., Gratton, R., D'Orazi, V., & Lucatello, S. 2009, A&A, 508, 695
Casamiquela, L., Soubiran, C., Jofré, P., et al. 2021, A&A, 652, A25
Castro-Ginard, A., Jordi, C., Luri, X., et al. 2022, A&A, 661, A118
Cescutti, G., & Chiappini, C. 2014, A&A, 565, A51
Cescutti, G., Chiappini, C., Hirschi, R., Meynet, G., & Frischknecht, U. 2013, A&A, 553, A51
Cescutti, G., Romano, D., Matteucci, F., Chiappini, C., & Hirschi, R. 2015, A&A, 577, A139
Clayton, D. D., & Rassbach, M. E. 1967, ApJ, 148, 69
Contursi, G., de Laverny, P., Recio-Blanco, A., & Palicio, P. A. 2021, A&A, 654, A130
Cristallo, S., Straniero, O., Gallino, R., et al. 2009, ApJ, 696, 797
Cristallo, S., Piersanti, L., Straniero, O., et al. 2011, ApJS, 197, 17
Cropper, M., Katz, D., Sartoretti, P., et al. 2018, A&A, 616, A5
da Silva, R., Lemasle, B., Bono, G., et al. 2016, A&A, 586, A125
De Cia, A., Jenkins, E. B., Fox, A. J., et al. 2021, Nature, 597, 206
Delgado Mena, E., Tsantaki, M., Adibekyan, V. Z., et al. 2017, A&A, 606, A94
Feuillet, D. K., Feltzing, S., Sahlholdt, C. L., & Casagrande, L. 2020, MNRAS, 497, 109
Feuillet, D. K., Sahlholdt, C. L., Feltzing, S., & Casagrande, L. 2021, MNRAS, 508, 1489
Forsberg, R., Jönsson, H., Ryde, N., & Matteucci, F. 2019, A&A, 631, A113
Freiburghaus, C., Rosswog, S., & Thielemann, F. K. 1999, ApJ, 525, L121
Frischknecht, U., Hirschi, R., & Thielemann, F. K. 2012, A&A, 538, L2
Frischknecht, U., Hirschi, R., Pignatari, M., et al. 2016, MNRAS, 456, 1803
Gaia Collaboration (Recio-Blanco, A., et al.) 2023a, A&A, in press https://doi.org/10.1051/0004-6361/202243511
Gaia Collaboration (Vallenari, A., et al.) 2023b, A&A, in press https://doi.org/10.1051/0004-6361/202243940
Gallino, R., Arlandini, C., Busso, M., et al. 1998, ApJ, 497, 388
Grevesse, N., Asplund, M., & Sauval, A. J. 2007, Space Sec. Rev., 130, 105
Grevesse, N., Scott, P., Asplund, M., & Sauval, A. J. 2015, A&A, 573, A27
Griffith, E., Weinberg, D. H., Johnson, J. A., et al. 2021, ApJ, 909, 77
Grisoni, V., Spitoni, E., Matteucci, F., et al. 2017, MNRAS, 472, 3637
Grisoni, V., Cescutti, G., Matteucci, F., et al. 2020, MNRAS, 492, 2828
Gull, M., Frebel, A., Hinojosa, K., et al. 2021, ApJ, 912, 52
Harris, W. E. 1996, AJ, 112, 1487
Helmi, A. 2020, ARA&A, 58, 205
Helmi, A., White, S. D. M., de Zeeuw, P. T., & Zhao, H. 1999, Nature, 402, 53
Helmi, A., Babusiaux, C., Koppelman, H. H., et al. 2018, Nature, 563, 85
Ishigaki, M. N., Aoki, W., & Chiba, M. 2013, ApJ, 771, 67
Kappeler, F., Beer, H., & Wisshak, K. 1989, Rep. Prog. Phys., 52, 945

Karakas, A. I., & Lattanzio, J. C. 2014, PASA, 31, e030
Katz, D., Sartoretti, P., Guerrier, A., et al. 2023, A&A, in press https://doi.org/10.1051/0004-6361/202244220
Koppelman, H. H., Helmi, A., Massari, D., Price-Whelan, A. M., & Starkenburg, T. K. 2019, A&A, 631, L9
Lamb, S. A., Howard, W. M., Truran, J. W., & Iben, I. 1977, J., ApJ, 217, 213
Lawler, J. E., Sneden, C., Cowan, J. J., Ivans, I. I., & Den Hartog, E. A. 2009, ApJS, 182, 51
Limongi, M., & Chieffi, A. 2018, ApJS, 237, 13
Magrini, L., Spina, L., Randich, S., et al. 2018, A&A, 617, A106
Maiorca, E., Randich, S., Busso, M., Magrini, L., & Palmerini, S. 2011, ApJ, 736, 120
Mashonkina, L. I., Vinogradova, A. B., Ptitsyn, D. A., Khokhlova, V. S., & Chernetsova, T. A. 2007, Astron. Rep., 51, 903
Matsuno, T., Hirai, Y., Tarumi, Y., et al. 2021, A&A, 650, A110
Matteucci, F., Romano, D., Arcones, A., Korobkin, O., & Rosswog, S. 2014, MNRAS, 438, 2177
Mishenina, T. V., & Kovtyukh, V. V. 2001, A&A, 370, 951
Mishenina, T. V., Pignatari, M., Korotin, S. A., et al. 2013, A&A, 552, A128
Myeong, G. C., Evans, N. W., Belokurov, V., Amorisco, N. C., & Koposov, S. E. 2018, MNRAS, 475, 1537
Nishimura, S., Kotake, K., Hashimoto, M.-A., et al. 2006, ApJ, 642, 410
Palicio, P. A., Recio-Blanco, A., Poggio, E., et al. 2023, A&A, 670, L7
Peters, J. G. 1968, ApJ, 154, 225
Pignatari, M., Gallino, R., Heil, M., et al. 2010, ApJ, 710, 1557
Poggio, E., Recio-Blanco, A., Palicio, P. A., et al. 2022, A&A, 666, L4
Prantzos, N., Abia, C., Limongi, M., Chieffi, A., & Cristallo, S. 2018, MNRAS, 476, 3432
Recio-Blanco, A., de Laverny, P., Allende Prieto, C., et al. 2016, A&A, 585, A93
Recio-Blanco, A., Fernández-Alvar, E., de Laverny, P., et al. 2021, A&A, 648, A108
Recio-Blanco, A., de Laverny, P., Palicio, P. A., et al. 2023, A&A, in press https://doi.org/10.1051/0004-6361/202243750
Reddy, A. B. S., Giridhar, S., & Lambert, D. L. 2012, MNRAS, 419, 1350
Reddy, B. E., Lambert, D. L., & Allende Prieto, C. 2006, MNRAS, 367, 1329
Rizzuti, F., Cescutti, G., Matteucci, F., et al. 2019, MNRAS, 489, 5244
Ruiz-Lara, T., Gallart, C., Bernard, E. J., & Cassisi, S. 2020, Nat. Astron., 4, 965
Sales-Silva, J. V., Daflon, S., Cunha, K., et al. 2022, ApJ, 926, 154
Santos-Peral, P., Recio-Blanco, A., de Laverny, P., Fernández-Alvar, E., & Ordenovic, C. 2020, A&A, 639, A140
Sheffield, A. A., Majewski, S. R., Johnston, K. V., et al. 2012, ApJ, 761, 161
Sneden, C., Cowan, J. J., & Gallino, R. 2008, ARA&A, 46, 241
Spina, L., Nordlander, T., Casey, A. R., et al. 2020, ApJ, 895, 52
Spina, L., Ting, Y. S., De Silva, G. M., et al. 2021, MNRAS, 503, 3279
Spitoni, E., Verma, K., Silva Aguirre, V., & Calura, F. 2020, A&A, 635, A58
Spitoni, E., Verma, K., Silva Aguirre, V., et al. 2021, A&A, 647, A73
Spitoni, E., Recio-Blanco, A., de Laverny, P., et al. 2023, A&A, in press https://doi.org/10.1051/0004-6361/202244349
Surman, R., McLaughlin, G. C., Ruffert, M., Janka, H. T., & Hix, W. R. 2008, ApJ, 679, L117
Tarricq, Y., Soubiran, C., Casamiquela, L., et al. 2021, A&A, 647, A19
Tautvaišienė, G., Viscasillas Vázquez, C., Mikolaitis, Š., et al. 2021, A&A, 649, A126
Travaglio, C., Gallino, R., Busso, M., & Gratton, R. 2001, ApJ, 549, 346
Vincenzo, F., & Kobayashi, C. 2020, MNRAS, 496, 80
Woosley, S. E., Wilson, J. R., Mathews, G. J., Hoffman, R. D., & Meyer, B. S. 1994, ApJ, 433, 229
Yong, D., Karakas, A. I., Lambert, D. L., Chieffi, A., & Limongi, M. 2008, ApJ, 689, 1031

Appendix A: ADQL queries

```
SELECT source_id
FROM gaiadr3.astrophysical_parameters inner join
    gaiadr3.gaia_source using(source_id)
WHERE
(rv_expected_sig_to_noise>0)
AND
(vbroad<=13)
AND
(teff_gspspec IS NOT NULL)
AND
(flags_gspspec LIKE '0%')
AND
(flags_gspspec LIKE '_0%')
AND
(flags_gspspec LIKE '__0%')
AND
(flags_gspspec LIKE '___0%')
AND
(flags_gspspec LIKE '____0%')
AND
(flags_gspspec LIKE '_____0%')
AND
(flags_gspspec LIKE '_____0%')
AND
((flags_gspspec LIKE '_____0%') OR (flags_gspspec
    LIKE '_____1%') )
AND
((flags_gspspec LIKE '_____0%') OR (
    flags_gspspec LIKE '_____1%') )
AND
((flags_gspspec LIKE '%0_____') OR (flags_gspspec
    LIKE '%1_____') OR (flags_gspspec LIKE
    '%2_____'))
AND
((flags_gspspec LIKE '%0____') OR (flags_gspspec LIKE
    '%1____') )
AND
(logchisq_gspspec<-3.75)
AND
(teff_gspspec<=5400)
AND
(logg_gspspec<=3.5)
AND
(cefe_gspspec IS NOT NULL)
AND
( (cefe_gspspec_upper-cefe_gspspec_lower)<=0.4)
```
Listing 1. `ADQL` query for the *low-uncertainty sample*.

Appendix B: Open cluster data

Table B.1. Mean of [Fe/H], [Ce/Fe], [Ca/Fe] for our 52 open clusters.

Cluster Name	Stars	[Fe/H]	[Ce/Fe]	[Ca/Fe]
Alessi Teutsch 8	1	-0.170	-0.110	-0.140
Stock 2	8	-0.131	-0.081	0.229
UBC 394	1	-0.290	-0.050	0.000
NGC 2632	3	0.120	-0.133	0.177
Alessi 44	1	-0.170	-0.110	0.020
Roslund 7	1	-0.200	-0.130	-0.200
COIN-Gaia 30	1	-0.300	-0.070	0.120
Trumpler 2	2	-0.265	-0.065	-0.070
UPK 431	1	-0.190	-0.080	0.020
NGC 2281	1	-0.250	-0.070	0.150
IC 2488	1	-0.230	-0.080	-0.010
NGC 5316	1	-0.210	-0.050	-0.100
NGC 2168	2	-0.140	-0.035	-0.010
ASCC 111	1	0.000	0.090	0.280
ASCC 11	1	-0.300	-0.070	0.030
NGC 2682	1	-0.290	0.080	0.150
NGC 5749	1	-0.290	-0.060	-0.120
NGC 2477	1	-0.360	0.060	0.070
NGC 7082	1	-0.220	-0.130	-0.170
NGC 2506	1	-0.650	0.150	0.350
NGC 6633	1	-0.240	-0.060	0.100
UPK 167	1	-0.150	-0.140	-0.180
NGC 2669	1	-0.180	-0.030	-0.050
ASCC 23	1	-0.190	-0.080	0.060
UPK 53	1	-0.180	-0.120	-0.060
Alessi Teutsch 11	1	-0.190	-0.060	0.150
UBC 4	1	-0.230	-0.060	0.170
NGC 1750	2	-0.245	-0.075	-0.080
NGC 1545	2	-0.300	-0.045	0.005
ASCC 71	1	-0.260	-0.110	-0.120
NGC 6475	2	-0.115	-0.090	-0.130
COIN-Gaia 26	1	-0.180	-0.120	0.000
NGC 6124	5	-0.218	-0.094	-0.086
NGC 2447	2	-0.355	-0.015	0.005
NGC 2287	2	-0.255	-0.070	-0.030
NGC 3532	3	-0.190	-0.080	0.140
Stock 1	1	0.030	-0.110	0.110
Collinder 350	1	-0.290	-0.030	0.030
NGC 5662	1	-0.320	-0.060	0.000
NGC 3114	3	-0.223	-0.163	-0.037
UPK 7	1	-0.220	-0.030	-0.080
NGC 6819	1	-0.350	0.180	0.500
Ruprecht 147	2	-0.075	-0.065	0.125
NGC 6281	2	-0.160	-0.065	0.070
NGC 1662	1	-0.230	-0.060	0.090
Platais 8	1	-0.040	-0.090	0.280
UBC 183	2	-0.295	-0.050	-0.025
Gulliver 21	1	-0.010	-0.120	-0.230
IC 4725	1	-0.050	0.030	-0.120
NGC 7789	2	-0.435	0.105	0.230
Collinder 258	1	-0.300	-0.040	0.200
NGC 1647	1	-0.240	-0.100	-0.140
Collinder 463	2	-0.180	-0.125	-0.085

Notes. The number of the stars from which we computed these mean values is indicated in the first column.